Characterisation of the filter inlet system on the BAE-146 research aircraft and its use for size resolved aerosol composition measurements

Alberto Sanchez-Marroquin[1], Duncan H. P. Hedges[1], Matthew Hiscock[2], Simon T. Parker[3], Philip D. Rosenberg[1], Jamie Trembath[4], Richard Walshaw[1], Ian T. Burke[1], James B. McQuaid[1], Benjamin J. Murray[1]

[1]School of Earth and Environment, University of Leeds, Woodhouse Lane, Leeds, LS2 9JT, UK

[2] Oxford Instruments NanoAnalysis, High Wycombe, HP12 3SE

[3]Defence Science and Technology Laboratory, Salisbury, SP4 0JQ, UK

[4]Facility for Airborne Atmospheric Measurements, Building 146, Cranfield University, College Road, Cranfield, Bedford MK43 0AL

Abstract

Atmospheric aerosol particles are important for our planet's climate because they interact with radiation and clouds. Hence, having characterised methods to collect aerosol from aircraft for detailed offline analysis are valuable. However, collecting aerosol, particularly coarse mode aerosol, onto substrates from a fast moving aircraft is challenging and can result in both losses and enhancement in particles. Here we present the characterisation of an inlet system designed for collection of aerosol onto filters on board the Facility for Airborne Atmospheric Measurements (FAAM) BAe-146 research aircraft. We also present an offline Scanning Electron Microscopy (SEM) technique for quantifying both the size distribution and size resolved composition of the collected aerosol. We use this SEM technique in parallel with online underwing optical probes in order to experimentally characterise the efficiency of the inlet system. We find that the coarse mode aerosol is sub-isokinetically enhanced, with a peak enhancement at around 10 μm up to a factor of three under typical operating conditions. Calculations show that the efficiency of collection then decreases rapidly at larger sizes. In order to minimise the isokinetic enhancement of coarse mode aerosol we recommend sampling with total flow rates above 50 L min^{-1}; operating the inlet with the bypass fully open helps achieve this by increasing the flow rate through the inlet nozzle. With the inlet characterised, we also present single particle chemical information obtained from X-ray spectroscopy analysis which allows us to group the particles into composition categories.

1 Introduction

Atmospheric aerosol particles are known to have an important effect on climate through directly scattering or absorbing solar and terrestrial radiation as well as through indirect effects such as acting as Cloud Condensation Nuclei (CCN) or Ice-Nucleating Particles (INPs) (Albrecht, 1989; DeMott et al., 2010; Haywood and Boucher, 2000; Hoose and Mohler, 2012; Lohmann and Diehl, 2006; Lohmann and Gasparini, 2017). Aerosol particles across the fine (diameter < 2 μm) and coarse (> 2 μm) modes are important for these atmospheric processes. For example, aerosol in the accumulation mode are important CCN (Seinfeld and Pandis, 2006), whereas supermicron particles are thought to contribute substantially to the INP population (Creamean et al., 2018; Mason et al., 2016; Pruppacher and Klett, 1997). Hence, being able to sample across the fine and coarse modes is required to understand the role aerosol play in our atmosphere. However, sampling aerosol particles without biases can be challenging, this being especially so on a fast moving aircraft (Baumgardner et al., 2011; Baumgardner and Huebert, 1993; McMurry, 2000; Wendisch and Brenguier, 2013).

It is necessary to sample aerosol from aircraft because in many cases aircraft offers the only opportunity to study aerosol and aerosol-cloud interactions at cloud relevant altitudes (Wendisch and

44 Brenguier, 2013). However, the relatively high speeds involved present a set of unique challenges for
45 sampling aerosol particles. This is especially so for coarse mode aerosol which are prone to both losses
46 as well as enhancements because their high inertia inhibits their ability to follow the air stream lines
47 when they are distorted by the aircraft fuselage and the inlet (Brockmann, 2011; McMurry, 2000; von
48 der Weiden et al., 2009). Therefore, inlet design and characterisation becomes extremely important
49 when sampling aerosol particles.

50 In this study we characterise the inlet system used for collecting filter samples (known as the Filters
51 system) on board the UK's BAe-146-301 Atmospheric Research Aircraft, Facility for Airborne
52 Atmospheric Measurements (FAAM). This system has been used for many years, but its
53 characterisation has been limited (Chou et al., 2008; Price et al., 2018; Ryder et al., 2018; Young et al.,
54 2016). Our goal in this characterisation work was to define recommendations for the use of the inlet
55 system to minimise sampling biases and define the size limitation and the biases that exist. While the
56 filter samples could be used for a variety of offline analyses, we have done this characterisation with
57 two specific goals in mind: firstly, we want to use this inlet system for quantification of INP (the
58 technique for this analysis has been described previously (Price et al., 2018) and will not be further
59 discussed here); secondly, we have adapted and developed a technique for quantification of and the
60 size resolved composition of the samples using Scanning Electron Microscopy (SEM). We use this
61 technique in order to test the inlet efficiency. These experiments are underpinned by calculations
62 which elucidate how the biases are impacted by variables such as flow speed, angle of attack and use
63 of the bypass system. Finally we present an example of the use of the inlet for determining the size
64 resolved composition of an aerosol sample collected from the FAAM aircraft.

65 **2. Description and theoretical sampling characteristics of the filter inlet system on the Facility for**
66 **Airborne Atmospheric Measurements (FAAM) aircraft**

67 Ideally, aerosol particles would be sampled through inlets without enhancement or losses. However,
68 this is typically not the case when sampling from aircraft, hence it is important to know how the size
69 distribution of the aerosol particles is affected by the sampling. Generally, an aircraft moves at high
70 velocities with respect to the air mass that it is being sampled. During sampling on the FAAM aircraft
71 the indicated airspeed is 100 m s^{-1}, which yields to a true airspeed that fluctuates between 100 and
72 120 m s^{-1}. The air mass has to decelerate when passing through the inlet (Baumgardner and Huebert,
73 1993) and this tends to result in inertial enhancement of coarse mode aerosol. There are also losses
74 through the inlet system, for example, through inertial impaction at bends or gravitational settling in
75 horizontal sections of pipework. These inlet characteristics need to be considered if the subsequent
76 analysis of the aerosol samples is to be quantitative. In this section we first describe the existing inlet
77 system and then present theoretical calculations for the size dependent losses and enhancements.

78 **2.1 Description of the Filters system**

79 The FAAM BAe-146 aircraft has two identical inlets for sampling aerosol onto filters for offline analysis.
80 This inlet system was used to sample aerosol particles on board of the C-130 aircraft before being
81 installed on the FAAM BAe-146 (Andreae et al., 1988; Andreae et al., 2000; Talbot et al., 1990), and it
82 has been used to sample aerosol particles on the FAAM Bae-146 e.g. (Chou et al., 2008; Hand et al.,
83 2010; Price et al., 2018; Young et al., 2016). A diagram of the inlet system can be seen in Fig. 1. The
84 two parallel inlet and filter holder systems, which each have a nozzle whose curved leading edge
85 profile follows the criteria for aircraft engine intakes at low Mach numbers (low speeds when
86 compared with the speed of sound; for FAAM during sampling this is ~0.3), and it is designed to avoid
87 the distortion of the pressure field at the end of the nozzle, flow separation and turbulence (Andreae
88 et al., 1988; Talbot et al., 1990). The inlet has a bypass to remove water droplets or ice crystals through

89   inertial separation and also enhance the flow rate at the inlet nozzle (Talbot et al., 1990). The flow
90   through the bypass (bypass flow) can be regulated using a valve and it is driven passively by the
91   pressure differential between the ram pressure inlet and the Venturi effect on the exhaust. After
92   turning inside the aircraft, the airstream containing the aerosol particles continue through the filter
93   stack after passing a valve. The air flow through the filter (filter flow) is measured by a mass flow
94   meter, which measures the sampled air mass and reports it in equivalent liters at standard conditions
95   (273.15 k, 1013.529 hPa). The uncertainty for this flow meter is 1% of the full scale (400 L min^{-1}). The
96   effect of water vapour on the mass flow has not been corrected since its effect is negligible. The signal
97   is integrated by an electronics unit to give the total volume of air sampled for any given time period.
98   There is also a valve between the pump and the flow meter. The valve allows the inlet and pump to
99   be isolated from the filter holder when changing the filter. The system uses a double-flow side channel
100   vacuum pump model SAH55 made by Elmo Rietschle (Gardner Denver Inc.), aided by the ram effect
101   of the aircraft. The flow rate at the inlet nozzle (total flow) is the sum of the bypass flow and the filter
102   flow. The inlet nozzle is located at 19.5 cm of the aircraft fuselage, so the sampling is carried out in
103   the free stream, outside the boundary layer.

104

105   **2.2 Sampling efficiency**

106   We present theoretical estimates of the losses and enhancements due to aspiration, inlet inertial
107   deposition, turbulent inertial deposition, inertial deposition in bends and gravitational effects in Fig
108   2a. We used the term 'efficiency' to define the ratio between the number concentrations of particles
109   after they were perturbed relative to the unperturbed value. If the efficiency is above one, the number
110   of particles is enhanced whereas if it is below 1, particles are lost before they reach the filter.

111   The sampling efficiency of any inlet depends on the flow rates and the flow regime (laminar vs
112   turbulent), the pressure and the temperature. Filter flow rates for 0.4 µm polycarbonate filters
113   normally vary between 10 and 50 L min^{-1} depending on altitude (see section 2.3 for a discussion of
114   flow rates). The bypass flow rate (when it is fully open) can go up to 35 L min^{-1} at 30 m and 22 L min^{-1}
115   at 6 km (volumetric L at standard conditions: 273.15 k, 1013.529 hPa), but it is not measured routinely.
116   In the 2.5 cm diameter section of the inlet, just after the inlet nozzle, the Reynolds number (Re) is
117   below the turbulent regime threshold (Re > 4000) for flow rates below 65 L min^{-1}. For larger values of
118   Re, the flow starts becoming turbulent. At the inlet nozzle, where the diameter 0.7 cm, Re is above
119   4000 for flow rates above 20 L min^{-1}, so the flow is briefly in the turbulent regime at the inlet for most
120   sampling conditions. Fully characterising the losses and enhancements of aerosol particles passing
121   through the inlet is very challenging since there are several aerosol size dependent mechanisms that
122   can enhance or diminish the amount of aerosol particles that arrive at the filter.

123   Here we have considered the most important of these mechanisms (von der Weiden et al., 2009) in
124   order to estimate the inlet efficiency (see Fig. 2a) for a total flow rate of 50 L min^{-1} (all the flow rates
125   of our calculations are given in L min^{-1} at standard conditions: 273.15 k, 1013.529 hPa). These loss
126   mechanisms and their importance in this inlet system are defined as follows (a discussion on the
127   choice of equations, how they have been applied and the excluded mechanisms can be found in
128   Appendix A):

129   *Aspiration efficiency* has been calculated using the empirical equation as develop in Belyaev and Levin
130   (1972) and Belyaev and Levin (1974). As one can see in Fig. 2a this mechanism enhances aerosol
131   particles, tending to 1 for small diameters and to the ratio in between the air speed inside the nozzle
132   and outside the aircraft for large ones.

133 *Inlet inertial deposition* has been characterised using the equation given in Liu et al. (1989) which
134 quantifies this effect. In Fig. 2a one can see that it produces some losses, with a minimum efficiency
135 of down to 50% for sizes about 6 μm, without affecting the lower and upper limit of the aerosol size.

136 *Turbulent inertial deposition* occurs throughout the whole inlet system for flow rates above 65 L min^{-1}
137 and only occurs in the inlet nozzle for flow rates below this threshold. We have used the equation
138 given by Brockmann (2011) in order to account for this mechanism. In Fig. 2a one can see an example
139 of the turbulent inertial losses at the nozzle. This mechanism gradually decreases the efficiency for
140 aerosol particles above 5 μm.

141 *Bending inertial deposition* has been characterised using the equation given in (Brockmann, 2011).
142 This efficiency mechanism, which can be seen in Fig. 2a, adds a size cut off with a D50 value at ~25
143 μm.

144 *Gravitational settling* of aerosol particles was considered using the equations developed in Heyder
145 and Gebhart (1977) and Thomas (1958), as stated in Brockmann (2011). This efficiency mechanism
146 adds another size cut off with a D50 value of 35 μm, as one can see in Fig. 2a*.

147 *Diffusional efficiency and filter collection efficiency* have not been included in Fig. 2. The first
148 mechanism has been calculated using the analytical equation given by Gormley and Kennedy (1948),
149 but it is not shown since it is very close to 1 for all the considered size range. For the filter types and
150 pore sizes we used, filter collection efficiency is also close to a 100% across the relevant size range
151 (Lindsley, 2016; Soo et al., 2016).

152 *Anisoaxial losses* are losses produced by the fact that the inlet is not aligned with the velocity of the
153 air mass, being offset by an angle, θ (related to the angle of attack). The anisoaxial sampling can affect
154 the sub-isokinetic efficiency, but using the equations given by Hangal and Willeke (1990a), we
155 calculated that this effect is minimal for our conditions. In addition, anisoaxial sampling can lead to
156 inertial losses when particles impact the inner walls of the inlet. This phenomena has been quantified
157 using the equations in Hangal and Willeke (1990b) and the results can be seen in Fig. 3. As one can
158 see, this efficiency mechanism adds an additional cut off for large aerosol particles (with values of D50
159 down to ~20 μm), depending on the value of the sampling angle.

160 One can see all the efficiency mechanisms combined for four different flow rates in Fig. 2b. These have
161 been derived by multiplying all the efficiencies for the individual mechanisms. This overall efficiency
162 is the ratio between the particles that reach the filter and the particles in the ambient air. The
163 sampling efficiency for the submicron aerosol is close to 1. At sizes above 1 μm, the different loss
164 mechanisms become increasingly significant. For the range of flow rates considered, the efficiency
165 approaches zero between 20 and 50 μm, with D50 values in between ~13 and ~33 μm (although these
166 values could be lower under certain values of angles of attack if considering the anisoaxial losses of
167 from Fig. 3, which haven't been included). For the 80 L min^{-1} case, the flow is turbulent through all the
168 pipe, leading to enhanced losses of coarse aerosol particles which partially compensate the sub-
169 isokinetic enhancement of the system.

170 One can also see that the sub-isokinetic enhancement of large aerosol particles increases when
171 decreasing the flow rate of the system. This effect is about a factor 3.5 for 10 μm particles when
172 sampling at 15 L min^{-1}, but only a factor of two at 50 L min^{-1}. The sub-isokinetic enhancement can be
173 mitigated using the bypass, which enhances the flow through the nozzle. This can be seen in Fig. 2c
174 where one can see a comparison between the total efficiency of a 20 L min^{-1} flow rate through the
175 filters with no bypass flow and the same case when the bypass is open. Since the considered bypass
176 flow is comparable to the flow rate through the filters, the difference between the total flows for the

177 two cases is approximately a factor 2. As a consequence, the maximum sub-isokinetic enhancement
178 of large aerosol particles is almost a factor 2 larger when sampling with the bypass closed. Hence, the
179 sub-isokinetic enhancement can be reduced by keeping the bypass fully open.

180

181 **2.3 Sampling flow rate**

182 Here we show flow rate data from four field campaigns in order to examine how the flow rate of the
183 filter inlet system varied based on different factors. We have used the data collected during the ICE-D
184 campaign, in Cape Verde during August 2015 (Price et al., 2018). The rest of the data is from some
185 flight test carried out during 2017 and 2018, and three field campaigns. The first one was EMERGE,
186 based in south east England, in July 2017. The second one was VANAHAEIM, based in Iceland in
187 October 2017. The last campaign was MACSSIMIZE, based in Alaska in 2018. The flow rate of the inlet
188 system is known to vary with altitude, with a lower flow rate at high altitudes because of the reduced
189 pressure differential across the filter and the fact that the pump efficiency decreases at low pressure.
190 In addition, it changes depending on the filter type and the pore size.

191 In Fig. 4, where all the flow rate data has been presented, one can see that the flow rate tends to
192 decrease with altitude and change with filter type as expected, but the flow rates are not always
193 consistent for each altitude and filter type, varying up to a factor two for each filter
194 type/line/altitude/campaign. The filter type effect on flow rate can be seen in Fig. 4, where the
195 average flow rate for 0.4 µm polycarbonate filters is about twice the flow rate of the 0.45 µm PTFE
196 filters. In order to investigate the inconsistency in the flow rate at each altitude, we analysed the flow
197 rate data by comparing it with different parameters (ambient air and cabin temperature, ambient air
198 and cabin pressure, wind direction and speed with respect to the aircraft movement), but there was
199 no correlation with any of these variables. Different mesh supports were used, but this does not affect
200 the flow rate significantly according to some ground based tests. We checked the flow rate through
201 each sampling period and found it did not change over time on a particular filter set (even after
202 stopping the sampling and starting it again). In addition, we performed some tests on the ground and
203 during flights to study the effect of potential leaks by inserting paper disks of the same dimension as
204 the filters in the filter holders and found no evidence of leaks in the system.

205 We conclude that this variability in the flow rate comes from variability in the pump performance in
206 combination with subtle differences in individual filter pairs. The side displacement pump is not the
207 ideal pump for this system and operates at its maximum capacity. Hence, we suggest that to improve
208 the performance of the system that flow rates are actively controlled and also the side displacement
209 pump is replaced with a more appropriate design. This would also have the advantage that flow rates
210 would be maintained at smaller pressure drops and allow sampling at higher altitudes.

211

212 **3. FAAM underwing optical particle counters**

213 Later in the paper we compare results from the underwing optical particle counters with our electron
214 microscope derived size distributions, hence we describe the optical instruments here. The FAAM BAe-
215 146 aircraft operates underwing optical particle counters to measure aerosol size distributions. These
216 include the Passive Cavity Aerosol Spectrometer Probe 100-X (PCASP) and the Cloud Droplet Probe
217 (CDP). The PCASP measures particles with diameters in the approximate range 0.1-3 µm and the CDP
218 measures the particles with diameters in the range of 2-50 µm. These instruments are placed outside
219 the aircraft fuselage, below the wings. These instruments and the methods for calibration are
220 described in (Rosenberg et al., 2012). All the PCASP-CDP data shown here has been extracted from

the FAAM cloud datasets corresponding to each specific flight via the Centre for Environmental Data Analysis.

The instruments were calibrated and had optical property corrections applied as per Rosenberg et al. (2012). We used a refractive index of 1.56 + 0i and a spherical approximation (Mie theory) in the optical property corrections. In Fig. 5, one can see a sensitivity test on the refractive index value we used in order to examine how variability in refractive index affect the bin centres position, their width, and therefore the size distribution obtained from the PCASP and CDP. As one can see in Fig. 5a, modification of the real part of the refractive index from 1.5 to 1.7 can change the position of the PCASP bin centres up to a factor 1.5, but its effect on the CDP is not significant. When varying the imaginary part of the refractive index from 0 to 0.01, the bin centre positions of the first half of the range of the PCASP and CDP do not change but it can change the position of the bins of the end of the range of both instruments (less than a factor 1.5). However, for the purposes of this work, the differences produced by the variation in the refractive index are not large enough to modify the conclusions of the analysis, therefore we use a value of 1.56 + 0i.

The chosen refractive index range for this sensitivity analysis can be justified on the basis that the SEM compositional analysis showed that the composition of the aerosol samples used in this study was very heterogeneous, dominated by carbonaceous particles (biogenic, organic and black carbon) and with some contributions of mineral dust and other particle types. Values of the real part of the refractive index in the 1.5 to 1.6 range are compatible with sodium chloride and ammonium sulphate (Seinfeld and Pandis, 2006), as well as most mineral dusts (McConnell et al., 2010). The range is very close to values for the real part of the refractive index of organic carbon but below the values for black carbon (Kim et al., 2015). As a consequence, the refractive index choice might not be accurate for a black carbon dominated sample. However, black carbon is highly unlikely to dominate in the size range where a value of the real part of the refractive index of 1.7 dramatically changes the size distribution (diameters above 0.5 µm) (Seinfeld and Pandis, 2006), so our refractive index choice is valid. In Fig. 5b one can see that changing the imaginary part of the refractive index from 0 to 0.01 only produces small changes in the distribution. The imaginary part of the refractive index of many aerosol types as sodium chloride, sulphates and mineral dust falls within the shown range (Seinfeld and Pandis, 2006), (McConnell et al., 2010). For values of the imaginary part of the refractive index above 0.01 (not shown in the image), the size distribution dramatically changes for sizes above 1 µm (but not for smaller values of it), overlapping and disagreeing with the CDP. However, values above 0.01 in the imaginary part of the refractive index are only associated with strongly absorbing aerosol like black carbon, which will dominate only in the submicron sizes (Seinfeld and Pandis, 2006). The submicron part of the size distribution doesn't change for values of the imaginary part of the refractive index above 0.01, so our refractive index choice is still acceptable even for samples with significant contributions from black carbon in submicron sizes.

For the PCASP-CDP, we have considered two uncertainty sources. The first one is the Poisson counting uncertainty in the number of particles in each bin and the second one is the uncertainty in the bin width that is given by the applied optical property corrections. Both sources have been propagated in order to obtain the errors of dN/dlog$D$p and dA/dlog$D$p. The errors in the bin centre position were given by the calibration. In order to avoid the problems with the transition in between different gain stages in the PCASP, some bins were merged or eliminated (5 and 6 as well as 15 and 16 were merged, while the bin 30 was eliminated), as indicated by Rosenberg et al. (2012). Other uncertainties such as the refractive index assumption or particle shape effect, as well as the uncertainty in the bin position haven't been regarded in this study. Sampling biases haven't been quantified or corrected yet so they

266 haven't been included. The size distributions produced by the PCASP-CDP have been taken as a
267 reference value for the purposes of this study.

268

269 **4. Scanning Electron Microscopy technique for aerosol characterization**

270 Scanning Electron Microscopy is used in order to study composition and morphology of aerosol
271 particles, in a similar way to previous works such as Krejci et al. (2005), Kandler et al. (2007), Chou et
272 al. (2008), Kandler et al. (2011), Young et al. (2016), Price et al. (2018) and Ryder et al. (2018). We use
273 a Tescan VEGA3 XM scanning electron microscope (SEM) fitted with an X-max 150 SDD Energy-
274 Dispersive X-ray Spectroscopy (EDS) system controlled by an Aztec 3.3 software by Oxford
275 Instruments, at the Leeds Electron Microscopy and Spectroscopy Centre (LEMAS) at the University of
276 Leeds. In order to get data from thousands of particles in an efficient way, data collection was
277 controlled by the AztecFeature software expansion.

278 Aerosol particles were collected with the filter inlet of the FAAM aircraft on polycarbonate track
279 etched filters with 0.4 μm pores (Whatman, Nucleopore). Samples for SEM are usually coated with
280 conductive materials in order to prevent the accumulation of charging on the sample surface (Egerton,
281 2005). For aerosol studies, materials like gold (Hand et al., 2010), platinum (Chou et al., 2008), or
282 evaporated carbon (Krejci et al., 2005; Reid et al., 2003; Young et al., 2016) have been used. When it
283 comes to choosing which signal to detect, some previous studies used mainly backscattered electrons
284 (Gao et al., 2007; Kandler et al., 2007; Kandler et al., 2011; Kandler et al., 2018; Price et al., 2018; Reid
285 et al., 2003; Young et al., 2016) and some others choose secondary electrons (Hamacher-Barth et al.,
286 2013; Krejci et al., 2005). We started the development of this analysis using a carbon coating and the
287 backscattered electron detector. This technique produced reproducible images and almost no
288 artefacts from the pore edges, consistent with Gao et al. (2007). However, we noticed that we
289 sometimes undercounted a significant fraction of the small carbon based particles (this strongly
290 depended on the sample), which looked transparent under the backscattered electron imaging but
291 not under the secondary electron detector, as seen in Fig. 6. This likely happened because the contrast
292 in the secondary electron images mainly depends on the topography of the sample whereas the
293 contrast in the backscattered electron images depends on the mean atomic number of each sample
294 phase (Egerton, 2005). Since the polycarbonate filters are made of C and O, particles containing only
295 these elements in a similar proportion to the background did not exhibit a high contrast under the
296 backscattered electron detector (Laskin and Cowin, 2001). However, when using secondary electron
297 imaging with carbon coatings, images were less reproducible and contained artefacts from the pore
298 edges, probably resulting from charging or topographical effects. We found that coating the samples
299 with 30 nm of iridium helps to improve the secondary electron image reproducibility and reduced the
300 pore edge artefacts as well as allowing us to locate small organic particles. An increase in the size of
301 the particle as a consequence of the coating may introduce an uncertainty in the size of the smallest
302 particles. An additional advantage of using Ir is that the energy dispersive X-ray spectrum of Ir does
303 not overlap greatly with the elements of interest.

304 In the SEM the sample was positioned at a working distance of 15 mm. The SEM's electron beam had
305 an accelerating voltage of 20 KeV and a spot size chosen to produce the optimum number of input
306 counts in the EDS detector. Images are taken at two different magnifications with a pixel dwell time
307 of 10 μs and a resolution of 1024 x 960 pixels per image. High magnification images (40 nm per pixel
308 or smaller) were used to identify particles down to 0.3 or 0.2 μm depending on the sample, and
309 medium magnification images (about 140 nm per pixel) are used to identify particles down to 1 μm. A
310 brightness threshold with upper and lower limits that correspond to pixels of certain shades of grey

311 was manually adjusted for each image by the operator to discriminate particles from the background.
312 Based on the manually set brightness threshold, AztecFeature identified the pixels that fall within the
313 limits as aerosol particles and calculated several morphological properties of the particle as cross
314 sectional area, length, perimeter, aspect ratio, shape factor or equivalent circular diameter. The
315 equivalent circular diameter is defined as $\sqrt{(4\,A\,\pi^{-1})}$, where A the cross sectional area of the aerosol
316 particle. This equivalent circular diameter has not been corrected or transformed into an optical or
317 other equivalent diameter.

318 For this analysis we placed a section of the 47 mm filter on a 25 mm stub. In order to collect
319 morphological and chemical information from a few thousand particles, we only scanned a fraction of
320 the filter (typically up to 1% of the filter at low magnification and up to 0.01% for high magnification).
321 We collected information from 5 to 20 different areas, and each area consisted of a montage of several
322 SEM images. In Fig. 7 one can see the radial distribution of aerosol particles on top of a filter collected
323 using the inlet system. In spite of some fluctuations (which are up to a factor 3 and appear to be
324 random), one can see that the particles are homogenously distributed all over the central ~30 mm of
325 the filter. As a consequence, the areas were chosen by the user from all over the surface of the
326 selected fraction of the filter. Each area was selected in the software, manually adjusting the particle
327 detection threshold. The Z position of the stage was also adjusted manually for each image in order
328 to produce properly focused images. After doing this, the image scanning and EDS acquisition was
329 performed in an automated way. Morphological information was recorded for all particles with an
330 equivalent circular diameter greater than the specified size threshold (typically 0.2 or 0.3 µm).

331 EDS analysis was restricted to the first 12 or 15 particles detected in each image. This reduces the
332 likelihood of image defocusing over the SEM automated run. The software performed EDS in the
333 centre of the particles, obtaining around 50,000 counts per particle. The raw data for any given particle
334 were matrix corrected and normalised by the AZtec software to produce element weight percent
335 values with a sum total of 100%, using a value of the confidence interval of 2 (a further discussion on
336 the confidence interval can be seen in the Appendix C). Then particles were categorised based on their
337 chemical composition using a classification scheme which can be created and modified within the
338 AztecFeature software. The characteristic X-rays taken at one point are emitted by a certain
339 interaction volume which is bigger than some of the analysed particles (typically < 2 μm^3, decreasing
340 with atomic number and increasing with incident electron energy). As a consequence, a part of the X-
341 ray counts attributed to each particle come from the background (C and O from the polycarbonate
342 filter and Ir from the coating) and the weight percentages obtained from the X-ray spectra do not
343 match the actual weight percentages of the particle itself. As a consequence, when categorising the
344 particles based on their composition, we only use the presence or absence of certain elements, and
345 the ratio between the weight percentages of non-background elements. The classification scheme
346 works by checking if the composition of each particle falls within a range of values which are manually
347 defined by the user. Particles not matching the first set of rules are tested again for a second set of
348 rules, and so on, until reaching the last set of rules. A few sets of rules can be merged into a category.
349 In the supplementary information (Fig. S3), we give the details of the 32 sets of rules used, which are
350 then summarised into 10 composition categories. A description of the most abundant elements in
351 each category and an interpretation of these categories is included in Appendix B.

352 The detection of particles has certain limitations. The edges of the pores can look brighter than the
353 rest of the filter in the SE images (probably because they consist of a larger surface area from which
354 secondary electrons can be generated, hence a larger signal). As a consequence, they can look like
355 ~0.2 µm particles, which is the main reason why particles below 0.3-0.2 µm (depending on the sample)
356 are not included in this analysis. These artefacts had a chemical composition similar to the filter, so

they were labelled as "Carbonaceous" by the classification scheme, falling at the same category as most biogenic and black carbon particles. However, these artefacts were only around 1 to 10 percent depending on the sample. If they appear in larger quantities, they can be removed manually after or during the analysis. Another limitation arises from the fact that some aerosol particles did not have sufficient brightness in the SE image and were not detected as a particle. This happens more frequently for submicron particles (especially the ones closer to the limit of detection), but it can also happen with some coarse mode aerosol particles, particularly if they are only composed of Na and Cl or S. This issue can be addressed if necessary by setting a very low limit of detection, which adds lots of artefacts as well as the low brightness particles, and then removing the artefacts manually (the artefacts can be easily identified by the user). In other infrequent instances, only a fraction of the particle had a brightness above the threshold, so they were detected as a smaller particle or multiple smaller particles, or if two particles are close enough, they can be detected as a single larger particle. However, we feel that in the vast majority of the cases a representative cross sectional area of the particle was picked by the software.

Blank polycarbonate filters can contain some particles on them from manufacturing or transport before being exposed to the air. In addition, handling and preparing the filters can introduce additional particles to it. In order to assess these artefacts, we scanned a few clean blank filters. We also examined a filter that had been brought to the flight, loaded in the inlet system (but not exposed to a flow of air), and then stored at -18 ^{o}C for a few months (like most of the aerosol samples on filters). The results of both the handling blank and the blank can be seen in Fig. S2. The number of particles is typically about the order of magnitude of one particle per 100 by 100 µm square, which is more than an order of magnitude below all the samples in this study (apart from the sample shown in Fig 9c which was taken in a very low aerosol environment, where it is only about a factor 2). In Fig. S2 one can see that about half of particles found in both blank filters and the handling blank belong to the metal rich category. However, further examination of the composition of these metal rich particles revealed that almost all of them were Cr rich particles (about 97 % in the case of the blank filters and about 96% in the case of the handling blank). As a consequence, we excluded all the Cr rich particles from the analysis of atmospheric aerosol. By doing this, we make sure that we exclude about half of the artefacts of the analysis. There was a contribution of mineral dust origin particles (Al-Si rich, SI rich and Si only) for sizes in between 0.7 and 5 µm in the handling blank (less than 10% of the number in the handling blanks). Generally, the composition of the particles present in the blank filters and in the handling blank was very similar, suggesting that most of these artefacts are not produced by the loading, manipulation and storage of the filter.

5. Inlet characterisation and sampling efficiency using Scanning Electron Microscopy

In order to experimentally test the inlet efficiency, to complement the efficiency calculations presented in Section 2.2, we have used SEM to quantify the size distribution of particles collected on filters (Sect. 4) and compare this with the measurements from the under-wing optical probes (Sect. 3). The calculations in Sect. 2.2 suggest that there is an enhancement of the coarse mode aerosol particles, which is larger when sampling with the bypass closed. To test this we have collected aerosol onto 0.4 µm pore size polycarbonate filter in both lines in parallel and show these results in Fig. 8. In one of the lines, the bypass was kept open, and in other line the bypass was kept closed. Using our SEM approach described in the Sect. 4, we calculated the size distribution of the aerosol particles on top of each filter. We compared these size distributions with the ones measured by the underwing optical probes (PCASP-CDP), as described in Sect. 3. We performed the comparison twice in two different test flights based in the UK.

One can see that the concentration of aerosol particles measured by the SEM on the filters was higher than the particles detected by the optical probes for sizes above ~8 μm in Fig. 8 (reaching about an order of magnitude in number around 10 μm in both cases). These results are consistent with Price et al. (2018) and Ryder et al. (2018), where they observed an enhancement of coarse aerosol particles in mineral dust dominated samples collected close to Cape Verde. In addition, the enhancement was larger when sampling with the bypass closed (about a factor 2-3). The results of these comparisons are in qualitative agreement with the theoretical calculations in Sect. 2.2, i.e. that the sub-isokinetic enhancement is reduced with the bypass open.

After establishing that having the bypass open produces a more representative sampling of coarse mode aerosol we then had the bypass open for the subsequent sampling. In Fig. 9 we have presented some other bypass open SEM size distributions compared with the PCASP-CDP data from three different aerosol samples in contrasting locations. Since these data were taken during the scientific field campaigns and not test flights, we only collected one polycarbonate filter for SEM since the other line was used for INPs analysis on Teflon filters (not shown here). In Fig 9a, one can see a sample collected in the UK where there is an enhancement of the coarse mode which reaches almost an order of magnitude at 10 μm. The sample shown in Fig 9b was collected in Iceland, and the enhancement of coarse aerosols can be seen through most of its range, reaching even the first two bins of the submicron aerosol range. In Fig 9c one can see a sample collected in North Alaska where the coarse mode aerosol concentration was one to two orders lower than the examples from the UK and Iceland. In this case the SEM size distribution is only about a factor 2 above the size distribution of the handling blank, nevertheless the SEM and optical probes both produce similarly low numbers of coarse mode aerosol. The low number concentration results in the lack of data in the SEM above 7 μm and the large uncertainties in the PCASP-CDP above 1.5 μm. We do not observe a coarse mode enhancement in this sample, probably because of the low aerosol concentration in the size range where we expect the largest biases and large uncertainties.

In the submicron range, one can see that in all the comparisons shown in Fig. 8 and Fig. 9 there is sometimes an undercounting in the SEM size distribution when compared with the optical probes. Generally, the undercounting increases with decreasing size and reaches an order of magnitude or more, as one can see in Fig. 8, Fig. 9a and Fig. 9c; this is qualitatively similar to Young et al. (2016). There are several potential reasons for this. We can rule out particles simply being lost by passing through the 0.4 μm polycarbonate filters, since they are known have a high collection efficiency (Lindsley, 2016; Soo et al., 2016), although some of them might deposit inside the pores and therefore not be detected. In addition, it is likely that some small particles are not sufficiently bright to be detected, despite the fact we made efforts to mitigate this problem with the use of secondary electrons and the Ir coating (see figure 6). Also, volatilization of certain types of aerosol particles (which are more abundant in the submicron fraction (Seinfeld and Pandis, 2006)) can occur during heating (in this case produced by deceleration of the flow in the inlet) or sampling (Bergin et al., 1997; Hyuk Kim, 2015; Nessler et al., 2003) and this effect could be enhanced by the fact that samples are exposed to high vacuum during the SEM analysis. In addition, the SEM techniques measure the dry diameter and the optical probes measure the aerosol diameter at ambient humidity. This hygroscopic effect shifts the dry size distributions to smaller sizes, which might also explain part of the disagreement (Nessler et al., 2003; Young et al., 2016). Disagreement in the measurements can also be produced by the fact that the techniques are measuring different diameters (optical and geometric).

Some of the PCASP size distributions contain some 'bumps' (particularly above 2 μm), but it is not possible to address if they are physical or just an artefact produced by the refractive index correction

449 (Rosenberg et al., 2012). Given the uncertainties on both techniques and the fact that they measure
450 different diameters (optical diameter in the case of the PCASP-CDP and geometric equivalent circular
451 diameter in the case of the SEM), this comparisons cannot be used to quantify the biases in the system,
452 but can be used to make a qualitative comparison. For similar reasons, the SEM data has not been
453 corrected using the theoretical efficiency.

6. Application to samples collected from the atmosphere above S.E. England and North Alaska

455 The SEM technique to produce size resolved composition of aerosol samples described in Sect. 4 has
456 been applied to samples collected from the FAAM aircraft in various locations. In Fig. 10 we show an
457 example of some of the capabilities of this technique applied to a sample collected in S. E. England.
458 The purpose of this section is purely to give examples of the capabilities of the technique, further
459 analysis is planned for subsequent papers. The fraction of particles corresponding to each
460 compositional category described in Appendix B for each size can be seen in Fig. 10a and the
461 corresponding number size distribution of each composition category can be seen in Fig. 10b. By
462 looking at this analysis, one can see that the sample carbonaceous aerosol particles made a substantial
463 contribution to the number across the full distribution and there was a clear mineral dust mode (Si
464 only, Si rich Al-Si rich and Ca rich) for particles larger than about 1 μm. There was also a smaller
465 contributions of metal rich and S rich aerosol particles, particularly in the fine mode. A potentially
466 useful application of the size resolved composition is calculating the surface area or mass of an
467 individual component of a heterogeneous aerosol. As an example, we have grouped the mineral dust
468 categories Si only, Si rich Al-Si rich and Ca rich to produce the surface area size distribution of mineral
469 dust (and potentially ash) in Fig. 10c.

470 In Fig. 11 we show six examples of the size-resolved composition of different aerosol samples in two
471 locations (South East England and North Alaska). We can see that the aerosol samples are very
472 different depending on the location. The aerosol samples collected in the UK shown in Fig 11a, c and
473 d are very similar to the sample shown in Fig. 10a. In fact the sample in Figure 10a was taken on the
474 same day in a similar location as the sample in Fig 11b and the similarity between the two helps to
475 demonstrate the reproducibility of our technique. Generally, these samples from S.E. England
476 contained carbonaceous aerosol throughout the size distribution, particularly in the fine mode. This
477 is consistent with typical urban influenced aerosol (Seinfeld and Pandis, 2006). There is also a
478 substantial proportion of mineral dust and only a small proportion of Na rich aerosol. In contrast, the
479 samples collected in North Alaska (close or above the Arctic Ocean) generally contained a smaller
480 proportion of carbonaceous particles, but much larger contributions of Na rich aerosol (very likely sea
481 salt particles, since they were collected in a marine environment). The S-rich category was also
482 substantial in the fine mode in Alaska, consistent with some samples collected in other areas of the
483 Arctic (Young et al., 2016), and some samples collected in a similar location (Creamean et al., 2018).
484 Notably, the coarse mode in Alaska, while generally smaller in number than in S.E. England, contained
485 a high proportion of mineral dusts. This is also consistent with other measurements in the Arctic
486 (Creamean et al., 2018; Young et al., 2016).

487

6. Recommendations for aerosol sampling with the Filters system on the FAAM aircraft

489 Based on the calculations in Sect. 2.1 and the experimental findings in the subsequent sections, we
490 suggest keeping the total flow rate (including the flow through the filters measured by the electronics
491 box plus the bypass flow, which can be between 20 and 35 L min^{-1}) above 50 L min^{-1}. Below this range,
492 the sub-isokinetic enhancement of large aerosol particles is above a factor 2, according to the

493   calculations in Sect. 2.2 that can be seen in Fig. 2b. For total flow rates above 65 L min^{-1}, the flow
494   becomes turbulent throughout the line, which associated losses. However, the calculations shown in
495   Fig. 2c indicate that the combination of the isokinetic enhancements and turbulent losses at 80 L min^{-}
496   ^{1} lead to a reasonably representative sampling, but when it reaches 150 L min^{-1}, the position of the
497   D50 drops to 6.5 μm (not shown in the graph) so such a high flow rate would not be appropriate if the
498   user wants to sample coarse aerosol particles. Hence, we recommend an operational upper limit of
499   80 L min^{-1}. For 0.45 μm PTFE filters and the 0.4 μm polycarbonate filters presented in Fig. 4, sampling
500   close to this flow rate range is often achievable by keeping the bypass open, since this increases the
501   total flow rate and brings it closer to the suggested range, as one can see in Fig. 2c. If other filter types
502   are used, the flow rates will be different to those presented here and these flow rates should be taken
503   in consideration when choosing the pore size (or equivalent pore size) in order to avoid dramatic
504   sampling biases.

505   We already mentioned in Sect. 2.3 that we recommend replacing the side displacement pump with a
506   design that would provide a greater pressure drop. In addition, we also recommend that the bypass
507   flow rate is also routinely measured and controlled in order that the flow at the inlet nozzle can be
508   optimised while sampling.

509

510   **9. Conclusions**

511   In this work we have characterised the filter inlet system on board the FAAM BAe-146 research aircraft
512   which is used for the collection of atmospheric aerosol particles for off line analysis. Our primary goal
513   is to use this inlet system for quantification of INP concentrations and size resolved composition
514   measurements, but it could also be used to derive other quantities with other analytical techniques.

515   In order to characterise the inlet system we made use of an electron microscope technique to study
516   the inlet efficiency, by comparing the SEM size distributions with the in situ size distributions
517   measured with underwing optical probes (PCASP-CDP). In spite of the discrepancies and uncertainties,
518   the sub-isokinetic enhancement of large aerosol particles predicted by the calculations in Sect. 2.2
519   was observed in these comparisons. We also experimentally verify that this enhancement is minimised
520   by operating the inlet with the bypass open which maximised the flow rate through the inlet nozzle.
521   In addition, we note that we performed tests with three very different aerosol distributions and the
522   size distribution of the particles on the filters had comparable features and concentrations to those
523   measured by the underwing optical probes. Overall, the inlet tends to enhance the concentration of
524   aerosol in the coarse mode with a peak enhancement at ~10 μm, but when operated with the
525   recommended flow conditions this enhancement is minimised. The inlet efficiency decreases rapidly
526   for sizes above about 20 μm and becomes highly dependent upon the specifics of the sampling such
527   as flow rates and angle of attack. Based on the calculations we recommend that the total flow rates
528   at the nozzle are maintained at between 50 and 80 l min^{-1}, and also that improvements are made to
529   the pump and bypass flow control (see Sect. 2.3).

530   We also established an SEM technique to determine the size resolved composition of the aerosol
531   sample. Each particle can be categorized based on its chemical composition using a custom made
532   classification scheme. Using this technique we showed that the filter system on board of the FAAM
533   BAe-146 spreads the particles evenly across the filter surface, which is necessary for the SEM size
534   distribution analysis.

535   Having a well characterised inlet allows us to sample aerosol particles up to around 20 μm with
536   knowledge of the likely biases from the aircraft. Hence, we can use this inlet system to collect aerosol

537   for offline analysis at altitudes which are relevant for clouds. For example, this may allow us to use the
538   size resolved aerosol composition to quantify the size distribution of individual aerosol components
539   at a particular location and combine this information with INP measurements to quantify the surface
540   area normalised ice nucleating ability of a specific class of aerosol.

541

Appendix A: discussion of the inlet efficiency calculations

Here we include a further description of the efficiency mechanisms used in the inlet model described in Fig. 2 and discuss the choice of the equations and their limits of validity:

Aspiration efficiency accounts for the fact that the speed of the sampled air mass (U_0), and the speed of the air through the beginning of the nozzle (U) are different. When these two speeds are equal, the sampling is called "isokinetic", whereas when the speeds don't match, the sampling is called super isokinetic or sub-isokinetic depending on if U_0 is smaller or larger than U respectively. In our case, the air mass moves at the flying speed, which varies with the altitude (110 m s^{-1} is a typical value for sampling altitudes), and the speed at the start of the inlet is almost always below 35 m s^{-1} (sub-isokinetic conditions). As a consequence, some air streamlines will be forced around the inlet, while high inertia particles won't, which will lead to an aspiration efficiency above 1 for coarse mode aerosol particles. This enhancement is greater for large particles due to their large inertia which makes difficult their ability to follow the air streamlines. The enhancement reaches a maximum value of U_0/U in its high diameter limit (when none of the particles in the sampled air mass follow the streamlines that escape from the inlet and all of them are sampled). The aspiration efficiency tends to 1 (no enhancement) for small diameters.

This behaviour has been characterised by several studies (we will only look at the sub-isokinetic range of the equations since it is impossible to reach the super isokinetic range during flight). An empirical equation was developed based on laboratory experiment by Belyaev and Levin (1972) and Belyaev and Levin (1974) (referred as B&L) for certain range of U/ U_0 ratio and Stokes number. However, for ratios below its experimental range (U/ U_0>0.2), the B&L function doesn't make physical sense since it converges to values above 1 for small particle sizes. The aircraft inlet system works at smaller U/ U_0 ratios sometimes, so this function is not very accurate to describe the behaviour of the system in such conditions. Liu et al. (1989) developed another function (referred as LZK) by means of a numerical simulation based on computational fluid mechanics. The U/ U_0 ratio and Stokes number valid range is wider than the B&L expression (down to 0.1). It agrees with the B&L expression in the U/ U_0 ratio the latter was developed for. For smaller values of the ratio, the LZK function are believed to be more accurate, since it predicts the known physical behaviour (no sub-isokinetic enhancement for small particle sizes). It reaches U/ U_0 ratios down to 0.2, which is enough to cover most of the total flow rates achieved in the inlet system. (Krämer and Afchine, 2004) developed another expression (referred as K&A) for 0.007< U/ U_0<0.2 based on computational fluid dynamics. However, for low particle sizes, the efficiency doesn't converge to 1. As a consequence, we have used the LZK (Liu et al., 1989) function since it covers most of the U/ U_0 ratios we get in the inlet system, it agrees with the experimental data in Belyaev and Levin (1972) and Belyaev and Levin (1974) and it converges to U_0/U for large particles sizes and 1 for small particle sizes. Outside its valid range (U / U_0 < 0.1), the LZK function agrees with the K&A function for large radius and converges to 1 for small particle sizes. The equation is valid for 0.01<Stks<100, which is enough to cover the range in between 1 and 100 µm. As already stated, it tends to 1 for small particles sizes and to U_0/U for large particles sizes (At 50 L min^{-1}, the ratio U/U_0 is 0.2). All the calculations were done under standard conditions (0 $^{\circ}$C and 1 bar). The effect of changes in pressure and temperature (and therefore air density and dynamic viscosity) that normally occur in the filter inlet system sampling range (0 to 3000 m), are negligible in all the used equations

The used equations (as well as the ones used for anisoaxial losses) have been developed for thin-walled nozzles, (this criteria was defined first in Belyaev and Levin (1974)). The inlet has been described as thin-walled in the literature (Andreae et al., 2000; Formenti et al., 2003; Talbot et al., 1990) but we haven't used this terminology here since it is not possible to numerically quantify this using the criteria given in (Belyaev and Levin, 1974) because the edge of the nozzle is curved. However,

588 the inlet has been designed to avoid distortion of the pressure field at the nozzle tip and the resulting
589 problems associated with flow separation and turbulence (Andreae et al., 1988) which is the main
590 caveat of inlet nozzles that are not thin-walled (Belyaev and Levin, 1974). As a consequence, we used
591 these sets of equations for thin-walled nozzles to describe the filter inlet system considered in this
592 study. The fact that the calculations done using this equations show that the filter inlet system has
593 biases with similar characteristics as the ones estimated experimentally for coarse aerosol particles
594 helps to support this assumption.

595 *Inlet inertial deposition i*s defined as the inertial loss of aerosol particles when they enter nozzle. It is
596 produced by the fact that the streamlines bend towards the walls at the moment they enter the
597 nozzle, some large inertia particles can impact the walls and get deposited. Here, we have used the
598 equation given in Liu et al. (1989) which quantifies this effect. It is also valid for 0.01<Stks<100, which
599 is enough to cover the range in between 1 and 100 μm.

600 *Turbulent inertial deposition* happens when some particles are collected by the wall when travelling
601 in a pipe in the turbulent regime because some of the particles cannot follow the eddies of the
602 turbulent flow. In order to include this mechanism, we used the equation given in Brockmann (2011),
603 using the relation in between the deposition velocity and dimensionless particle relaxation time given
604 by Liu and Ilori (1974). These calculations are valid for a cylindrical pipe, whereas the turbulent section
605 of the inlet considered here is the nozzle, which has a conical shape. In order to account for this, we
606 divided the conical nozzle into 90 conical sections with an increasing diameter and a length of 1mm,
607 and combined the effect of all the sections. This approach does not account for the additional inertial
608 losses that could occur as a consequence of the enlargement of the flow in the conical section. As
609 already mentioned, above 65 L min^{-1}, turbulent flow occurs in the whole inlet tube. This has been
610 taken into account in the 80 L min^{-1} case in Fig. 2b. The equation used here has been tested for size
611 ranges in between 1.4 and 20 μm, and doesn't depend on the Reynolds number values it was tested
612 for (10000 and 50000) (Liu and Ilori, 1974).

613 *Bending inertial deposition* was also considered, since the line curves with an angle of 45° in order to
614 bring the airstream into the cabin. The inertia of some particles may keep them in their original track
615 and they are not able to follow the air streamlines that are bending towards the cabin, following the
616 inlet tubes. In order to account for these losses, we have used the empirical equation given in
617 Brockmann (2011) based on the data from Pui et al. (1987) for laminar flow. This equation was
618 developed for Reynold numbers of 1000, and we have used it for higher values. However, in
619 Brockmann (2011), one can see that the data from Pui et al. (1987) for Re=6000 (beginning of the
620 turbulent flow regime) doesn't differ that much from the fit we have used (valid for Re=1000). Since
621 our Re numbers for the thick section of the tube almost never go above 5000, we can still use the
622 laminar flow fit. This model has been tested for 0.08 < Stks < 1.2, which is enough to cover most of the
623 range where the inertial deposition efficiency drops from 1 to 0. The main caveat of this calculation is
624 that the model considers a smooth tube where that the flow rate before and after the bending is the
625 same, while in the inlet system, if the bypass flow is on, the flow rate before and after the bending is
626 different (before it, it would be equal to the total flow rate, whereas after the bending, it would be
627 equal to the filter flow rate). As a consequence we assumed that the flow rate after the bending is
628 equal to the total flow rate. This assumption might underestimate the losses since some large aerosol
629 particles will become accumulated in the bypass.

630 *Gravitational settling* was also considered. We used the analytical equation given by Thomas (1958),
631 as stated in Brockmann (2011). We applied this equation for the section of the pipe from the nozzle
632 to the bend (15 cm long). We used the modification (also analytical) of the previous equation given in
633 Heyder and Gebhart (1977) in order to account for the losses in the second section of the tube which

634   is 40 cm long and it is bended 45°. The gravitational losses in the nozzle were neglected since the
635   settling distance is much shorter and the time the air takes to pass it is smaller since it travels quicker.
636   As stated previously, the lower part of the turbulent regime can be reached for high flow rates through
637   all the tube. For these cases, we still use this equation which is only valid for the laminar regime, since
638   the gravitational settling efficiencies for the turbulent regime are very close to the laminar regime
639   ones (Brockmann, 2011) and wouldn't make a significant difference in our calculations.

640   *Diffusional efficiency* accounts for the fact that small aerosol particles could diffuse to the walls of the
641   pipe via Brownian motion. In order to account for this phenomenon, we have used the analytic
642   equation by Gormley and Kennedy (1948) as stated in Brockmann (2011). We have assumed that
643   diffusion happens only in the tube (before and after the bend) and excluding the diffusion in the nozzle
644   since it is negligible because these losses are a function of the residence time and the residence time
645   of the aerosol particles in the nozzle is much smaller than the rest of the tube. F or this calculation,
646   we have assumed 0 °C and 1 atm. We didn't show the efficiency associated to diffusion in Fig. 2a
647   because it was very close to 1 for all considered sizes. It only becomes slightly smaller than 1 for sizes
648   below 20 nm at 50 L min^{-1}. As a consequence, the inlet could be potentially used to sample nucleation
649   mode aerosol particles, even though for this study we will only focus on the particles larger than 0.1
650   μm.

651   *Filter collection efficiency* accounts for the fact that some particles can pass through the pores of the
652   filter, if they are smaller than the pores. However, filter pore size (in the case of polycarbonate
653   capillarity filters) and filter equivalent pore size (in the case of PTFE porous filters) is sometimes
654   misunderstood as a size cut off at which smaller particles are lost and larger particles are captured.
655   However, particle collection on filters happens through several mechanisms including interception,
656   impaction, diffusion, gravitational settling or by electrostatic attraction under certain conditions
657   (Flagan and Seinfeld, 1988; Lee and Ramamurthi, 1993). As a consequence, particles with diameters
658   below the pore size are normally collected (Lindsley, 2016; Soo et al., 2016). 99.48% of the generated
659   sodium chloride particles with sizes in between 10.4 and 412 nm were collected by a 0.4 μm
660   polycarbonate filter at flow rates below 11.2 L min^{-1} (smaller than most of the flow rates at which the
661   air passes through the same filters in the FAAM filter inlet system) (Soo et al., 2016). As a consequence,
662   we assumed a filter collection efficiency of 100% across the whole considered size range (0.1 to 100
663   μm). However, the fact that some aerosol particles with diameters below the pore size could be
664   deposited in the filter pores and therefore not be detected by the SEM technique could contribute to
665   the undercounting.

666   *Anisoaxial losses* have not been considered in the analysis shown in Fig. 2, after estimating that they
667   would only affect particles significantly larger than 10 μm and the fact that the alignment of the inlet
668   is difficult to quantify and the angle of attack changes during the flight. Using the equations explained
669   in Hangal and Willeke (1990a), we calculated that the modification of the sub-isokinetic behaviour of
670   the inlet produced by small values of θ is negligible. The equation was used beyond its experimental
671   limit, but this extrapolation was justified by the fact that the equation for θ = 0 made asymptotic
672   physical sense at the low and high Stokes number limits and produced very similar results to the ones
673   showed in Fig. 2a. Anisoaxial sampling can also produce inertial losses when particles impact the walls
674   of the inlet. These ones have been quantified using the expression given by Hangal and Willeke
675   (1990b) for different values of θ and they can be seen in Fig. 3. This mechanism looks very similar to
676   the gravitational and bend deposition efficiency shown in Fig. 2a. Anisoaxial inertial losses add a cut
677   off that prevents large particles to be sampled. As one can see in Fig. 3, the effect is very dependent
678   on the angle and only affects particles significantly larger than 10 μm in most cases, so it hasn't been
679   included in the total analysis shown in the Fig 2. One can see in Fig. 3 that the position of the D50 of

680   the anisoaxial cut off decreases when increasing values of θ up to 2°. For values of θ between 2° and
681   6°, it increases when increasing θ.

682   *Other losses:* Some mechanisms (thermophoresis, diffusiophoresis, interception, coagulation and re-
683   entrainment of deposited particles) have not been considered, since they are second order
684   mechanisms under our conditions when compared with the calculated mechanisms (Brockmann,
685   2011; von der Weiden et al., 2009) and for one of them (electrostatic deposition) it is not possible to
686   quantify them. Electrostatic deposition is normally avoided by using grounded conductive materials
687   so no electrical field exists within the tubing (Brockmann, 2011). Since the FAAM BAe-146 research
688   aircraft is not grounded during the flight, we cannot state this mechanism is irrelevant. However, the
689   experimental agreement between the SEM and optical probes suggest that this is a minor loss
690   mechanism.

691

692   **Appendix B. SEM compositional categories**

693   Here we describe the 10 categories we have used in our compositional analysis, which are a summary
694   of the 32 rules described in the supplementary information. The approach has some similarities with
695   the ones in previous studies (Chou et al., 2008; Hand et al., 2010; Kandler et al., 2011; Krejci et al.,
696   2005; Young et al., 2016), but it is distinct. Because of the fact that the filter is made of C and O,
697   background elements (C and O) were detected in all the particles. Particles in each category can
698   contain smaller amounts of other elements apart from the specified ones. This classification scheme
699   has been designed a posteriori to categorise the vast majority of the aerosol particles in the three field
700   campaigns previously described and some ground collected samples in the UK and Barbados. The main
701   limitation of the classification scheme is the difficulty to categorise internally mixed particles. The
702   algorithm has been built in a way it can identify mixtures of mineral dust and sodium chloride (they
703   appear as mineral dust but they could be split into a different category if necessary) and sulphate or
704   nitrate ageing on sodium chloride (they appear as Na rich but it could also be split into a different
705   category). However, other mixtures of aerosol wouldn't be identified, and they would be categorised
706   by the main component in the internal mixture in most cases.

707   B.1. Carbonaceous

708   The particles in this category contained only background elements (C and O). The components of the
709   carbonaceous particles consist in either black carbon from combustion processes or organic material,
710   which can be either directly emitted from sources or produced by atmospheric reactions (Seinfeld and
711   Pandis, 2006). Particles containing certain amount of K and P in addition to the background elements
712   were also accepted in these category. These elements are consistent with biogenic origin aerosol
713   particles (Artaxo and Hansson, 1995). Distinction between organic and black carbon aerosol
714   unfortunately could not reliably be done. Since N is not analysed in our SEM set up, any nitrate aerosol
715   particle would fall into this category if it is on the filter. However, since these particles are semi-
716   volatile, some of these aerosol particles would not resist the low pressure of the SEM chamber. This
717   could be further investigated in the future.

718   B.2. S rich

719   Aerosol particles in this category contained a substantial amount of S. This S might be in the form of
720   inorganic or organic sulphate compounds. Some sulphate compounds, such as sulphuric acid, are
721   relatively volatile and will be lost in the SEM chamber.

722   B.3 Metal rich

723   The composition of particles in this category is dominated by one of the following metals: Fe, Cu, Pb,
724   Al, Ti, Zn or Mn. These EDS signatures are compatible with metallic oxides or other metal rich particles.
725   These metal containing particles can originate from both natural sources and anthropogenic sources.
726   Some metallic oxides are common crustal materials that could go into the atmosphere but are also
727   produced during some combustion processes (Seinfeld and Pandis, 2006). In addition, many types of
728   metal and metallic derivatives particles are produced as component of industrial emissions and other
729   anthropogenic activities (Buckle et al., 1986), (Fomba et al., 2015).

730   B.4. Na rich

731   Sodium chloride particles are the main component of the sea spray aerosol particles which are emitted
732   through wave breaking processes (Cochran et al., 2017). These particles can age in the atmosphere by
733   reacting with atmospheric components such as sulphuric or nitric acid (Graedel and Keene, 1995),
734   (Seinfeld and Pandis, 2006). As a consequence of this reaction, a part of their Cl content will end up in
735   the gaseous phase (as HCl), leading to an apparent chlorine deficit in the aged sea spray aerosol
736   particles. Particles in this category have an EDS signature compatible with sea spray aerosol particles
737   since they are identified by the presence of Na, containing in most cases Cl and/or S (N is not included
738   in our SEM analysis).

739   B.5 Cl rich

740   Particles in this category contained mainly Cl and sometimes also K but never Na, so they are not
741   sodium chlorine particles. Significant concentrations of Cl and metals in aerosol particles have been
742   linked to industrial activities, coal combustion, incineration and automobile emissions (Graedel and
743   Keene, 1995; Paciga et al., 1975), whereas Cl and K in aerosol particles could be originated by the use
744   of fertilisers (Angyal et al., 2010), biomass burning (Lieke et al., 2017; Zender et al., 2003), or emitted
745   during pyrotechnic events (Crespo et al., 2012).

746   B.6 Ca rich

747   The composition of the particles in this category is dominated by Ca. In this category, particles
748   containing only Ca (plus C and O, the background elements) are consistent with calcium carbonate, a
749   major component of mineral dust (Gibson et al., 2006). If other elements such as Mg and S are present,
750   the signature of the particles compatible with some mineral origin elements as gypsum and dolomite
751   respectively. In addition, presence of minor amounts of Si, Al and other elements could indicate mixing
752   of these Ca rich particles with some other soil components as silicates. However, since Ca is a biogenic
753   element, we cannot discard the biogenic origin of some of the Ca-rich particles (Krejci et al., 2005).
754   Some Ca rich particles could originate from the crystallization of sea water, loosely attached to NaCl.
755   The latter component would dominate over the rest of the elements of the conglomerate and they
756   would appear as Na rich particles, unless they shatter in the air (Hoornaert et al., 1996; Parungo et al.,
757   1986).

758

759   B.7 Al-Si rich

760   Particles in the Al-Si rich category were detected by the presence of Al and Si as major elements. Very
761   often, this particles also contained smaller amounts of Na, Mg, K, Ca, Ti, Mn and Fe. Particles in this
762   category are very likely to have mineral origin and are commonly described as aluminosilicates which
763   include a range of silicates such as feldspars and clays (Chou et al., 2008; Hand et al., 2010). Mixed
764   mineral origin particles containing both Al and Si can also fall into this category. Strong presence of Na

765 and Cl could indicate internal mixing with some sea spray aerosol, whereas a strong S presence could
766 indicate atmospheric acid ageing.

767 B.8 Si only

768 The particles in this category contained only Si apart from the background elements. Particles in this
769 category are very likely to be a silica polymorph (mainly quartz), one of the major components of the
770 earth's crust. Since we cannot determine if the C signal in the EDS of these particles is produced from
771 the background or from the particle itself, a particle containing only C, Si and O would fall into this
772 category, however, mineral phases containing these elements are extremely rare.

773 B.9 Si rich

774 The composition of these particles was dominated by Si, and other elements Na, Mg, K, Ca, Ti, Mn and
775 Fe. The main difference with the particles in B7 is that the ones described here didn't contain Al above
776 the limit of detection. The EDS signal of particles in this category is compatible with any silicate that
777 does not contain Al as a major component in its phase such as talc or olivine. The only exception is
778 quartz, which falls in the 'Si only' category described above. They could also be internal mixtures of
779 silica or silicates without aluminium as a major component in its phase. Because of the high limit of
780 detection of the Al (See the SI), some particles in this category could contain small amounts of Al, and
781 should belong to Al-Si rich category. As in the Al-Si rich particles case, strong presence of Na and Cl
782 could indicate internal mixing with some sea spray aerosol, whereas a strong S presence could indicate
783 atmospheric acid ageing.

784 Some of these categories could be further grouped. For example, the particles in the Ca rich, Al-Si
785 rich, Si only and Si rich categories could be considered as "mineral dust". However, if the sample
786 contains ash from combustion processes or volcanic origin, it will also appear in these last categories
787 since its composition is similar to mineral dust (Chen et al., 2012; Nakagawa and Ohba, 2003).

788

Appendix C. Weight percentage confidence level sensitivity test

The software calculates the weight percentage (wt %) of each detected element with its statistical error (σ). In our classification scheme, we have imposed the rule that all the detected elements must be statistically significant in order to be considered as present (the wt % of each detected element needs to be a certain confidence level above the σ. We explored the appropriate value of sigma for our application below.

Our analysis is distinguished from others in the literature in that we use a relatively thick Ir coating (30 nm) as well as a relatively low EDS integration time in order to get data from many particles in a session. Some of the secondary EDS peaks of Ir overlap in some cases with some of the atmospherically relevant elements (the primary peak does not). This produces some issues like a larger σ in some elements. This effect is quite noticeable for Al and S, where some clear peaks of these elements were not statistically significant at a confidence level of 3. In Fig. C1 we show the results of a test where we studied the effect of changing the confidence level from 3 to 2 σ in the particle categorisation carried out by the classification scheme. The only effect of this change yields on the Al and S. When going from 3 to 2 σ as a confidence level, more Al is detected in the sample, so some Si-rich particles (from rule 25) are detected as Al-Si rich particles (rule 5) instead. Manual inspection of a subset of these particles revealed that the Al peak that wasn't being identified at 3 σ is an actual Al signal that was detected at 2 σ. Likewise, some significant S peaks were not being detected at a confidence level of 3 σ but they were at 2 σ, leading to more S rich particles (rule 14) that were labelled as Other from the rule 32 at a higher confidence level. The variation in the confidence level didn't modify the number of particles in other categories, so we recommend the use a 2 σ value in order to minimise the underestimation of Al-Si and S rich particles.

Acknowledgements

We a grateful for helpful discussions with Paola Formenti (Centre National de la Recherche Scientifique), Hannah Price (FAAM) and Eduardo Morgado (School of Earth and Environment, University of Leeds). Airborne data were obtained using the FAAM BAe-146-301 Atmospheric Research Aircraft, flown by Airtask Ltd and managed by FAAM Airborne Laboratory, jointly operated by UKRI and the University of Leeds. We thank all the people involved in the EMERGE, VANAHEIM and MACSSIMIZE campaigns, as well as Avalon. We acknowledge the Leeds Electron Microscopy and Spectroscopy Centre for the use of their microscopy facilities and the Centre for Environmental Data Analysis for providing us with the FAAM datasets used here. We are grateful for funding from the European Research Council (ERC) (648661 MarineIce).

825 **References**

826 Albrecht, B. A.: Aerosols, cloud microphysics, and fractional cloudiness, Science, 245, 1227-1230, 1989.

827 Andreae, M. O., Berresheim, H., Andreae, T. W., Kritz, M. A., Bates, T. S., and Merrill, J. T.: Vertical-
828 Distribution of Dimethylsulfide, Sulfur-Dioxide, Aerosol Ions, and Radon over the Northeast Pacific-
829 Ocean, J. Atmos. Chem., 6, 149-173, 1988.

830 Andreae, M. O., Elbert, W., Gabriel, R., Johnson, D. W., Osborne, S., and Wood, R.: Soluble ion
831 chemistry of the atmospheric aerosol and SO2 concentrations over the eastern North Atlantic during
832 ACE-2, Tellus B, 52, 1066-1087, 2000.

833 Angyal, A., Kertész, Z., Szikszai, Z., and Szoboszlai, Z.: Study of Cl-containing urban aerosol particles by
834 ion beam analytical methods, Nucl. Instrum. Methods Phys. Res. B, 268, 2211-2215, 2010.

835 Artaxo, P. and Hansson, H. C.: Size Distribution of Biogenic Aerosol-Particles from the Amazon Basin,
836 Atmos. Environ., 29, 393-402, 1995.

837 Baumgardner, D., Brenguier, J. L., Bucholtz, A., Coe, H., DeMott, P., Garrett, T. J., Gayet, J. F., Hermann,
838 M., Heymsfield, A., Korolev, A., Kramer, M., Petzold, A., Strapp, W., Pilewskie, P., Taylor, J., Twohy, C.,
839 Wendisch, M., Bachalo, W., and Chuang, P.: Airborne instruments to measure atmospheric aerosol
840 particles, clouds and radiation: A cook's tour of mature and emerging technology, AtmRe, 102, 10-29,
841 2011.

842 Baumgardner, D. and Huebert, B.: The airborne aerosol inlet workshop: Meeting report, J. Aerosol Sci,
843 24, 835-846, 1993.

844 Belyaev, S. P. and Levin, L. M.: Investigation of aerosol aspiration by photographing particle tracks
845 under flash illumination, J. Aerosol Sci, 3, 127-140, 1972.

846 Belyaev, S. P. and Levin, L. M.: Techniques for collection of representative aerosol samples, J. Aerosol
847 Sci, 5, 325-338, 1974.

848 Bergin, M. H., Ogren, J. A., Schwartz, S. E., and McInnes, L. M.: Evaporation of ammonium nitrate
849 aerosol in a heated nephelometer: Implications for field measurements, Environ. Sci. Technol., 31,
850 2878-2883, 1997.

851 Brockmann, J. E.: Aerosol Transport in Sampling Lines and Inlets. In: Aerosol Measurement, John Wiley
852 & Sons, Inc., 2011.

853 Buckle, R., Tsakiropoulos, P., and C. Pointon, K.: Preparation and properties of metallic aerosol
854 particles, Int. Mater. Rev., 31, 258-288, 1986.

855 Chen, H., Laskin, A., Baltrusaitis, J., Gorski, C. A., Scherer, M. M., and Grassian, V. H.: Coal fly ash as a
856 source of iron in atmospheric dust, Environ. Sci. Technol., 46, 2112-2120, 2012.

857 Chou, C., Formenti, P., Maille, M., Ausset, P., Helas, G., Harrison, M., and Osborne, S.: Size distribution,
858 shape, and composition of mineral dust aerosols collected during the African Monsoon
859 Multidisciplinary Analysis Special Observation Period 0: Dust and Biomass-Burning Experiment field
860 campaign in Niger, January 2006, J. Geophys. Res. Atmos., 113, 1-17, 2008.

861 Cochran, R. E., Ryder, O. S., Grassian, V. H., and Prather, K. A.: Sea Spray Aerosol: The Chemical Link
862 between the Oceans, Atmosphere, and Climate, Acc. Chem. Res., 50, 599-604, 2017.

863 Creamean, J. M., Kirpes, R. M., Pratt, K. A., Spada, N. J., Maahn, M., de Boer, G., Schnell, R. C., and
864 China, S.: Marine and terrestrial influences on ice nucleating particles during continuous springtime
865 measurements in an Arctic oilfield location, Atmos. Chem. Phys, 18, 18023-18042, 2018.

866 Crespo, J., Yubero, E., Nicolas, J. F., Lucarelli, F., Nava, S., Chiari, M., and Calzolai, G.: High-time
867 resolution and size-segregated elemental composition in high-intensity pyrotechnic exposures, J.
868 Hazard. Mater., 241-242, 82-91, 2012.

869 DeMott, P. J., Prenni, A. J., Liu, X., Kreidenweis, S. M., Petters, M. D., Twohy, C. H., Richardson, M. S.,
870 Eidhammer, T., and Rogers, D. C.: Predicting global atmospheric ice nuclei distributions and their
871 impacts on climate, Proc Natl Acad Sci U S A, 107, 11217-11222, 2010.

872 Egerton, R. F.: Physical principles of electron microscopy, Springer US, 2005.

873 Flagan, R. C. and Seinfeld, J. H.: Removal of particles from gas streams. In: Fundamentals of Air
874 Pollution Engineering, Prentice-Hall, Inc., Englewood Cliffs, NJ, 1988.

875 Fomba, K. W., van Pinxteren, D., Muller, K., Iinuma, Y., Lee, T., Collett, J. L., and Herrmann, H.: Trace
876 metal characterization of aerosol particles and cloud water during HCCT 2010, Atmos. Chem. Phys, 15,
877 8751-8765, 2015.

878 Formenti, P., Elbert, W., Maenhaut, W., Haywood, J., and Andreae, M. O.: Chemical composition of
879 mineral dust aerosol during the Saharan Dust Experiment (SHADE) airborne campaign in the Cape
880 Verde region, September 2000, J. Geophys. Res., 108, 8576, 2003.

881 Gao, Y., Anderson, J. R., and Hua, X.: Dust characteristics over the North Pacific observed through
882 shipboard measurements during the ACE-Asia experiment, Atmos. Environ., 41, 7907-7922, 2007.

883 Gibson, E. R., Hudson, P. K., and Grassian, V. H.: Aerosol chemistry and climate: Laboratory studies of
884 the carbonate component of mineral dust and its reaction products, Geophys Res Lett, 33, 1-5, 2006.

885 Gormley, P. G. and Kennedy, M.: Diffusion from a Stream Flowing through a Cylindrical Tube, Math.
886 Proc. Royal Ir. Acad., 52, 163-169, 1948.

887 Graedel, T. E. and Keene, W. C.: Tropospheric budget of reactive chlorine, Global Biogeochem. Cycles,
888 9, 47-77, 1995.

889 Hamacher-Barth, E., Jansson, K., and Leck, C.: A method for sizing submicrometer particles in air
890 collected on Formvar films and imaged by scanning electron microscope, Atmos. Meas. Tech., 6, 3459-
891 3475, 2013.

892 Hand, V. L., Capes, G., Vaughan, D. J., Formenti, P., Haywood, J. M., and Coe, H.: Evidence of internal
893 mixing of African dust and biomass burning particles by individual particle analysis using electron
894 beam techniques, J. Geophys. Res., 115, 1-11, 2010.

895 Hangal, S. and Willeke, K.: Aspiration efficiency: unified model for all forward sampling angles, Environ.
896 Sci. Technol., 24, 688-691, 1990a.

897 Hangal, S. and Willeke, K.: Overall Efficiency of Tubular Inlets Sampling at 0-90 Degrees from Horizontal
898 Aerosol Flows, Atmos Environ a-Gen, 24, 2379-2386, 1990b.

899 Haywood, J. and Boucher, O.: Estimates of the direct and indirect radiative forcing due to tropospheric
900 aerosols: A review, Rev Geophys, 38, 513-543, 2000.

901   Heyder, J. and Gebhart, J.: Gravitational deposition of particles from laminar aerosol flow through
902   inclined circular tubes, J. Aerosol Sci, 8, 289-295, 1977.

903   Hoornaert, S., Van Malderen, H., and Van Grieken, R.: Gypsum and Other Calcium-Rich Aerosol
904   Particles above the North Sea, Environ. Sci. Technol., 30, 1515-1520, 1996.

905   Hoose, C. and Mohler, O.: Heterogeneous ice nucleation on atmospheric aerosols: a review of results
906   from laboratory experiments, Atmos. Chem. Phys, 12, 9817-9854, 2012.

907   Hyuk Kim, C.: Characterization of Volatilization of Filter-Sampled PM2.5 Semi-Volatile Inorganic Ions
908   Using a Backup Filter and Denuders, Aerosol Air Qual. Res., 2015, 2015.

909   Kandler, K., Benker, N., Bundke, U., Cuevas, E., Ebert, M., Knippertz, P., Rodríguez, S., Schütz, L., and
910   Weinbruch, S.: Chemical composition and complex refractive index of Saharan Mineral Dust at Izaña,
911   Tenerife (Spain) derived by electron microscopy, Atmos. Environ., 41, 8058-8074, 2007.

912   Kandler, K., Lieke, K., Benker, N., Emmel, C., Kupper, M., Muller-Ebert, D., Ebert, M., Scheuvens, D.,
913   Schladitz, A., Schutz, L., and Weinbruch, S.: Electron microscopy of particles collected at Praia, Cape
914   Verde, during the Saharan Mineral Dust Experiment: particle chemistry, shape, mixing state and
915   complex refractive index, Tellus B, 63, 475-496, 2011.

916   Kandler, K., Schneiders, K., Ebert, M., Hartmann, M., Weinbruch, S., Prass, M., and Pohlker, C.:
917   Composition and mixing state of atmospheric aerosols determined by electron microscopy: method
918   development and application to aged Saharan dust deposition in the Caribbean boundary layer,
919   Atmos. Chem. Phys, 18, 13429-13455, 2018.

920   Kim, J., Bauer, H., Dobovicnik, T., Hitzenberger, R., Lottin, D., Ferry, D., and Petzold, A.: Assessing
921   Optical Properties and Refractive Index of Combustion Aerosol Particles Through Combined
922   Experimental and Modeling Studies, Aerosol Sci. Technol., 49, 340-350, 2015.

923   Krämer, M. and Afchine, A.: Sampling characteristics of inlets operated at low U/U0 ratios: new
924   insights from computational fluid dynamics (CFX) modeling, J. Aerosol Sci, 35, 683-694, 2004.

925   Krejci, R., Strom, J., de Reus, M., and Sahle, W.: Single particle analysis of the accumulation mode
926   aerosol over the northeast Amazonian tropical rain forest, Surinam, South America, Atmos. Chem.
927   Phys, 5, 3331-3344, 2005.

928   Laskin, A. and Cowin, J. P.: Automated single-particle SEM/EDX analysis of submicrometer particles
929   down to 0.1 μm, Anal Chem, 73, 1023-1029, 2001.

930   Lee, K. W. and Ramamurthi, M.: Chapter 10: Filter Collection. In: Aerosol Measurement: Principles,
931   Techniques, and Applications

932   Willeke, K. and Baron, P. (Eds.), Van Nostrand Reinhold, New York, 1993.

933   Lieke, K., Kandler, K., Scheuvens, D., Emmel, C., Glahn, C. V., Petzold, A., Weinzierl, B., Veira, A., Ebert,
934   M., Weinbruch, S., and Schütz, L.: Particle chemical properties in the vertical column based on aircraft
935   observations in the vicinity of Cape Verde Islands, Tellus B: Chemical and Physical Meteorology, 63,
936   497-511, 2017.

937   Lindsley, W. G.: Filter Pore Size and Aerosol Sample Collection, NIOSH Manual of Analytical Methods,
938   2016. 1-14, 2016.

Liu, B. Y. H. and Ilori, T. A.: Aerosol deposition in turbulent pipe flow, Environ. Sci. Technol., 8, 351-356, 1974.

Liu, B. Y. H., Zhang, Z. Q., and Kuehn, T. H.: A Numerical Study of Inertial Errors in Anisokinetic Sampling, J. Aerosol Sci, 20, 367-380, 1989.

Lohmann, U. and Diehl, K.: Sensitivity Studies of the Importance of Dust Ice Nuclei for the Indirect Aerosol Effect on Stratiform Mixed-Phase Clouds, J. Atmospheric Sci., 63, 968-982, 2006.

Lohmann, U. and Gasparini, B.: A cirrus cloud climate dial?, Science, 357, 248-249, 2017.

Mason, R. H., Si, M., Chou, C., Irish, V. E., Dickie, R., Elizondo, P., Wong, R., Brintnell, M., Elsasser, M., Lassar, W. M., Pierce, K. M., Leaitch, W. R., MacDonald, A. M., Platt, A., Toom-Sauntry, D., Sarda-Esteve, R., Schiller, C. L., Suski, K. J., Hill, T. C. J., Abbatt, J. P. D., Huffman, J. A., DeMott, P. J., and Bertram, A. K.: Size-resolved measurements of ice-nucleating particles at six locations in North America and one in Europe, Atmos. Chem. Phys, 16, 1637-1651, 2016.

McConnell, C. L., Formenti, P., Highwood, E. J., and Harrison, M. A. J.: Using aircraft measurements to determine the refractive index of Saharan dust during the DODO Experiments, Atmos. Chem. Phys, 10, 3081-3098, 2010.

McMurry, P.: A review of atmospheric aerosol measurements, Atmos. Environ., 34, 1959-1999, 2000.

Nakagawa, M. and Ohba, T.: Minerals in Volcanic Ash 1: Primary Minerals and Volcanic Glass, Global Environ. Res., 6, 2003.

Nessler, R., Bukowiecki, N., Henning, S., Weingartner, E., Calpini, B., and Baltensperger, U.: Simultaneous dry and ambient measurements of aerosol size distributions at the Jungfraujoch, Tellus B, 55, 808-819, 2003.

Paciga, J. J., Roberts, T. M., and Jervis, R. E.: Particle-Size Distributions of Lead, Bromine, and Chlorine in Urban-Industrial Aerosols, Environ. Sci. Technol., 9, 1141-1144, 1975.

Parungo, F. P., Nagamoto, C. T., and Harris, J. M.: Temporal and spatial variations of marine aerosols over the Atlantic Ocean, AtmRe, 20, 23-37, 1986.

Price, H. C., Baustian, K. J., McQuaid, J. B., Blyth, A., Bower, K. N., Choularton, T., Cotton, R. J., Cui, Z., Field, P. R., Gallagher, M., Hawker, R., Merrington, A., Miltenberger, A., Neely Iii, R. R., Parker, S. T., Rosenberg, P. D., Taylor, J. W., Trembath, J., Vergara-Temprado, J., Whale, T. F., Wilson, T. W., Young, G., and Murray, B. J.: Atmospheric Ice-Nucleating Particles in the Dusty Tropical Atlantic, J. Geophys. Res. Atmos., 123, 2175-2193, 2018.

Pruppacher, H. R. and Klett, J. D.: Microphysics of Clouds and Precipitation Dordrecht: Kluwer Academic Publishers, 1997.

Pui, D. Y. H., Romay-Novas, F., and Liu, B. Y. H.: Experimental Study of Particle Deposition in Bends of Circular Cross Section, Aerosol Sci. Technol., 7, 301-315, 1987.

Reid, E. A., Reid, J. S., Meier, M. M., Dunlap, M. R., Cliff, S. S., Broumas, A., Perry, K., and Maring, H.: Characterization of African dust transported to Puerto Rico by individual particle and size segregated bulk analysis, J. Geophys. Res. Atmos., 108, -, 2003.

Rosenberg, P. D., Dean, A. R., Williams, P. I., Dorsey, J. R., Minikin, A., Pickering, M. A., and Petzold, A.: Particle sizing calibration with refractive index correction for light scattering optical particle counters

978 and impacts upon PCASP and CDP data collected during the Fennec campaign, Atmos. Meas. Tech., 5,
979 1147-1163, 2012.

980 Ryder, C. L., Marenco, F., Brooke, J. K., Estelles, V., Cotton, R., Formenti, P., McQuaid, J. B., Price, H. C.,
981 Liu, D. T., Ausset, P., Rosenberg, P. D., Taylor, J. W., Choularton, T., Bower, K., Coe, H., Gallagher, M.,
982 Crosier, J., Lloyd, G., Highwood, E. J., and Murray, B. J.: Coarse-mode mineral dust size distributions,
983 composition and optical properties from AER-D aircraft measurements over the tropical eastern
984 Atlantic, Atmos. Chem. Phys, 18, 17225-17257, 2018.

985 Seinfeld, J. H. and Pandis, S. N.: Atmospheric Chemistry and Physics: From Air Pollution to Climate
986 Change, Wiley, 2006.

987 Soo, J. C., Monaghan, K., Lee, T., Kashon, M., and Harper, M.: Air sampling filtration media: Collection
988 efficiency for respirable size-selective sampling, Aerosol Sci Technol, 50, 76-87, 2016.

989 Talbot, R. W., Andreae, M. O., Berresheim, H., Artaxo, P., Garstang, M., Harriss, R. C., Beecher, K. M.,
990 and Li, S. M.: Aerosol Chemistry during the Wet Season in Central Amazonia - the Influence of Long-
991 Range Transport, J. Geophys. Res. Atmos., 95, 16955-16969, 1990.

992 Thomas, J. W.: Gravity Settling of Particles in a Horizontal Tube, J. Air Pollut. Control Assoc., 8, 32-34,
993 1958.

994 von der Weiden, S. L., Drewnick, F., and Borrmann, S.: Particle Loss Calculator – a new software tool
995 for the assessment of the performance of aerosol inlet systems, Atmos. Meas. Tech., 2, 479-494, 2009.

996 Wendisch, M. and Brenguier, J. L.: Airborne Measurements for Environmental Research: Methods and
997 Instruments, 2013.

998 Young, G., Jones, H. M., Darbyshire, E., Baustian, K. J., McQuaid, J. B., Bower, K. N., Connolly, P. J.,
999 Gallagher, M. W., and Choularton, T. W.: Size-segregated compositional analysis of aerosol particles
1000 collected in the European Arctic during the ACCACIA campaign, Atmos. Chem. Phys, 16, 4063-4079,
1001 2016.

1002 Zender, C. S., Bian, H. S., and Newman, D.: Mineral Dust Entrainment and Deposition (DEAD) model:
1003 Description and 1990s dust climatology, Journal of Geophysical Research-Atmospheres, 108, 2003.

1004

 Figures
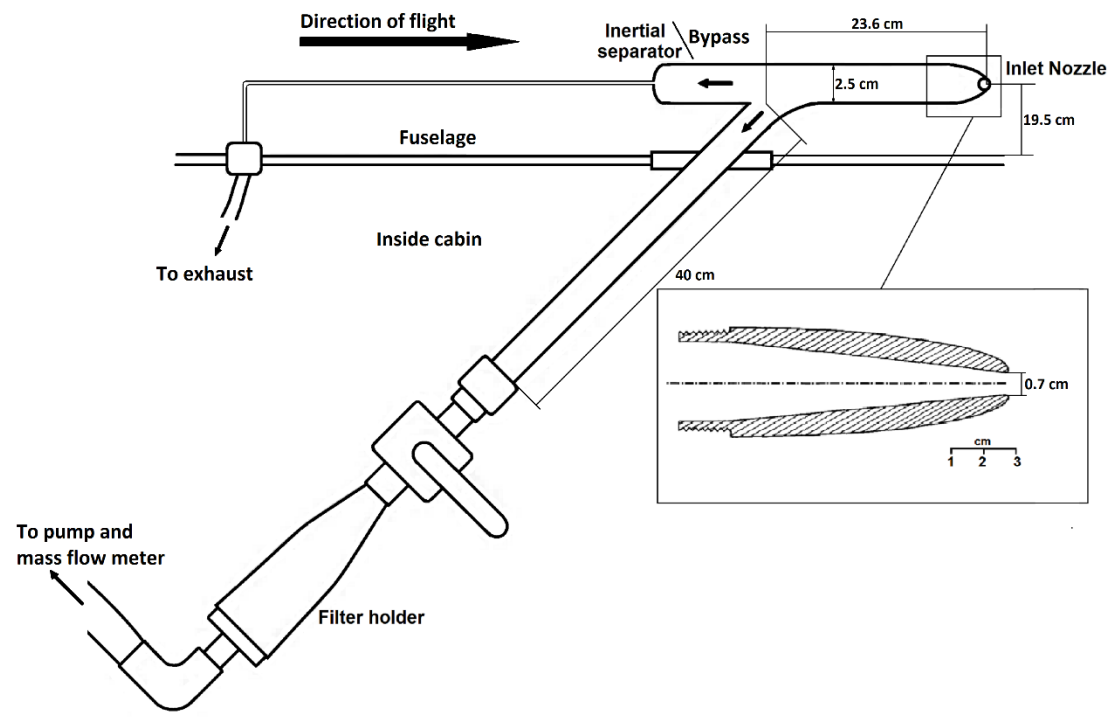
1007   Fig. 1. Schematic diagram of one of the two parallel lines of the Filters inlet system.

1008

1009

1010
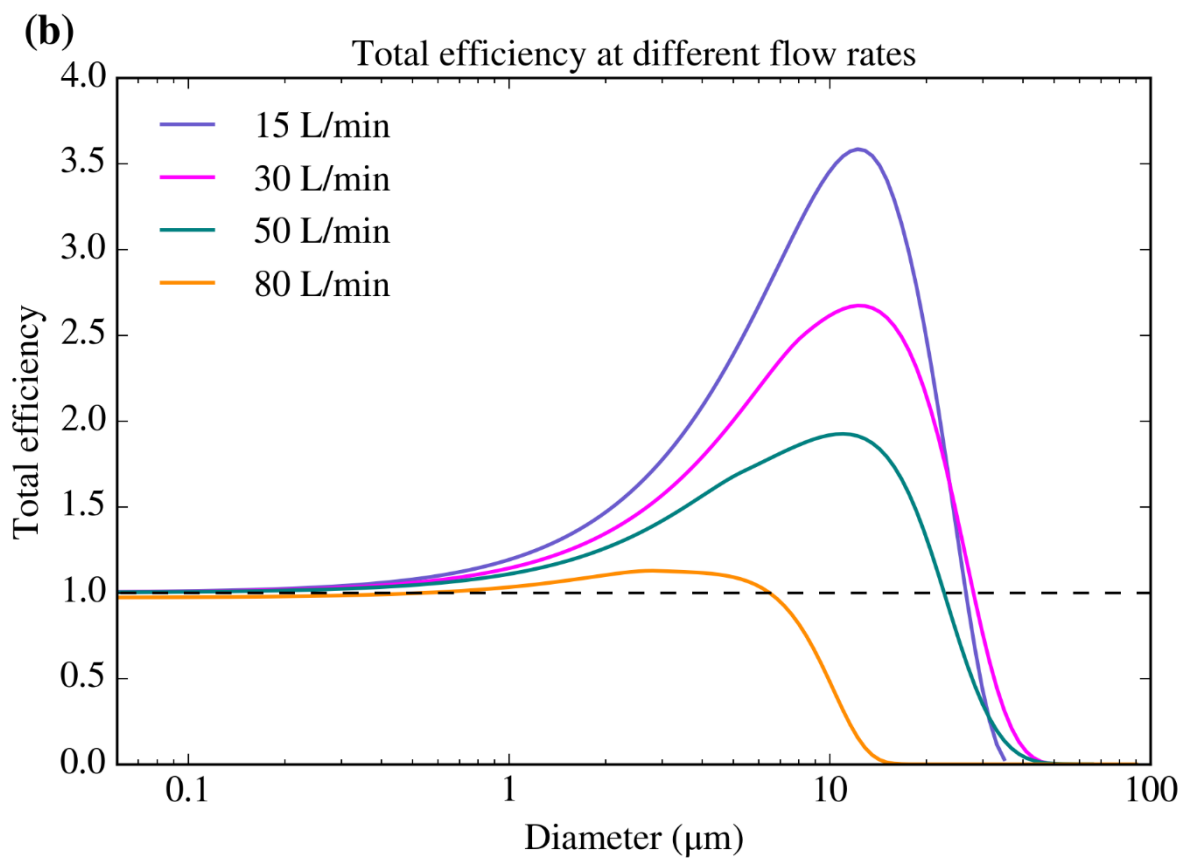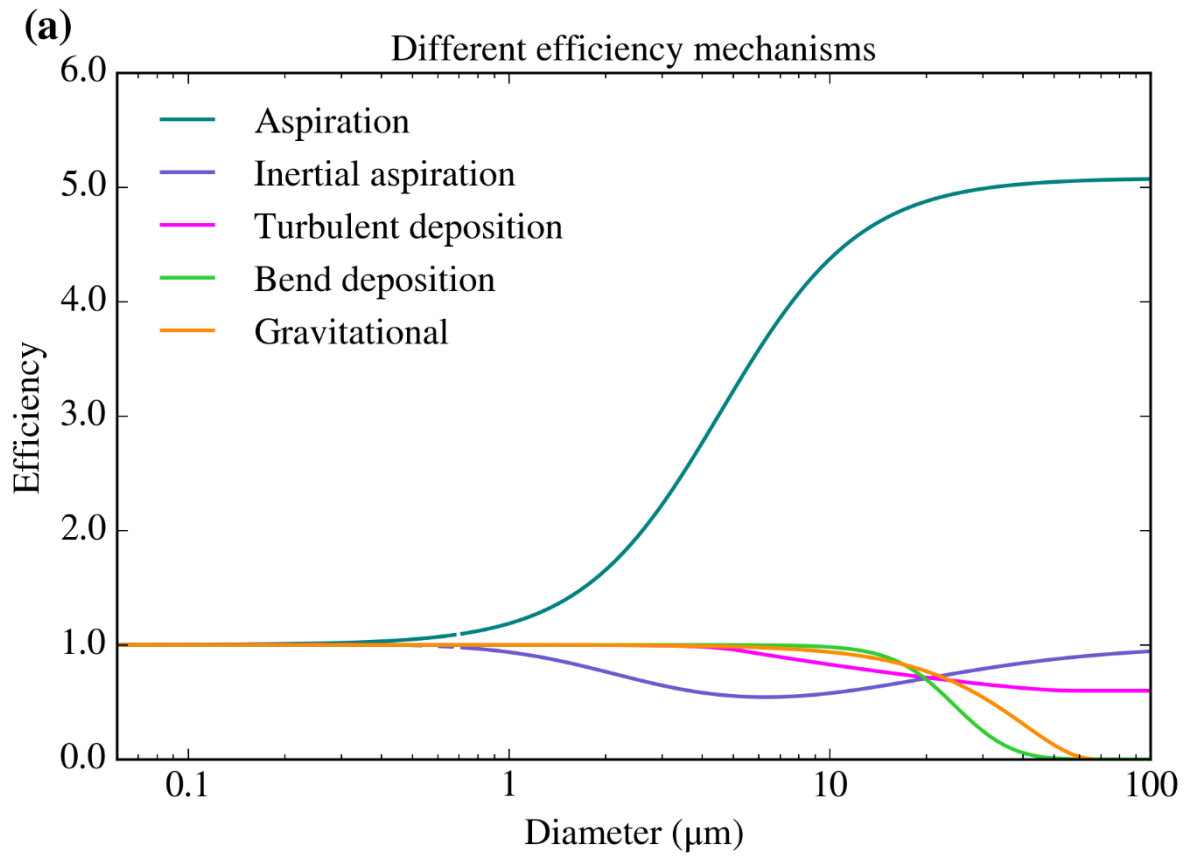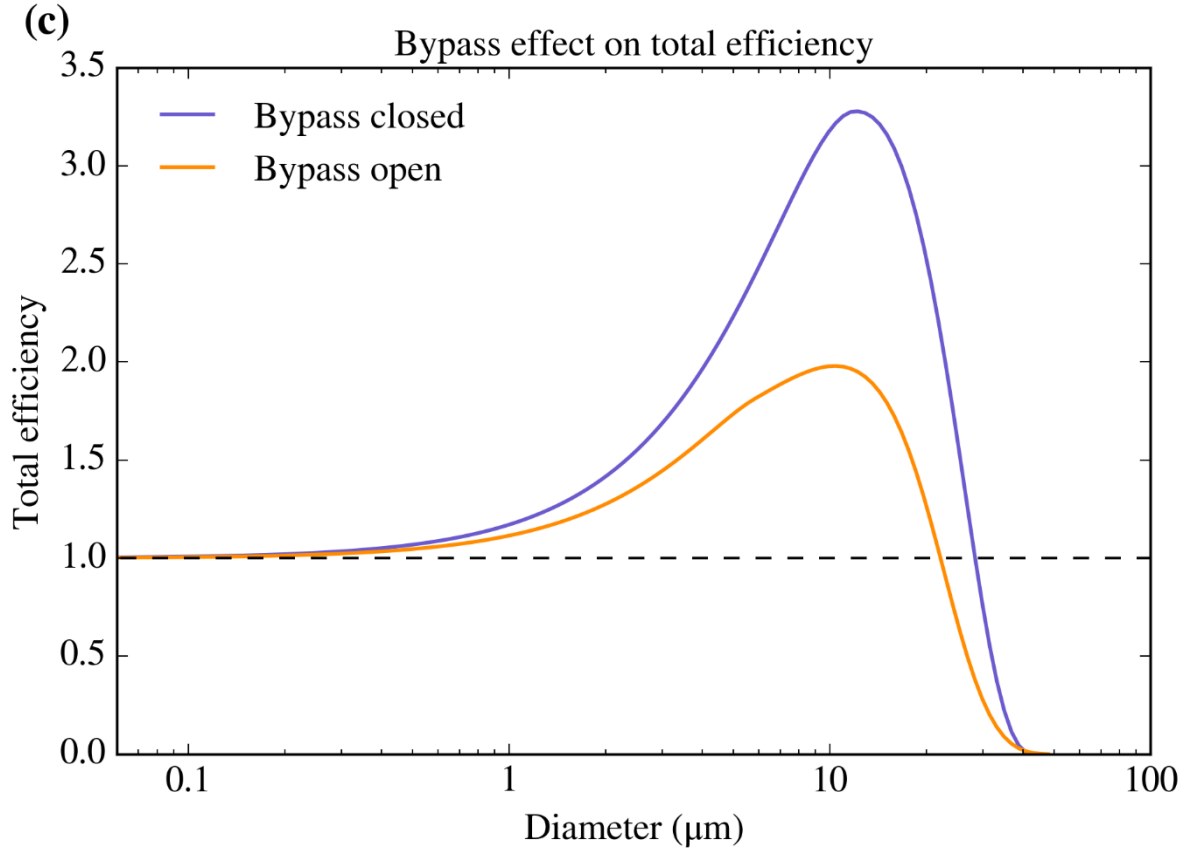
1011   Fig. 2. *Theoretical efficiencies of the Filter inlet system.* (a) Efficiencies of the four mechanisms considered in this work for a
1012   total flow rate of 50 L min^{-1}. We have assumed a dynamic viscosity of 1.82x10^{-5} kg m^{-1} s^{-1} (value for 0 ^{o}C) and a particle density
1013   of 1000 kg m^{-3}. The speed of the air mass (U$_0$) was 110 m s^{-1}, a typical FAAM flying speed at low altitudes. (b) Total efficiency
1014   for four different total flow rates. For the 80 L min^{-1} case, turbulent deposition through the whole line was considered since
1015   the flow was turbulent through the whole pipe. (c) Total efficiency considering all the described mechanisms for a 20 L min^{-1}
1016   filter flow rate with the bypass closed and a 20 L min^{-1} filter flow rate with the bypass open (considering a bypass flow of 25
1017   L min^{-1}).

1018

1019
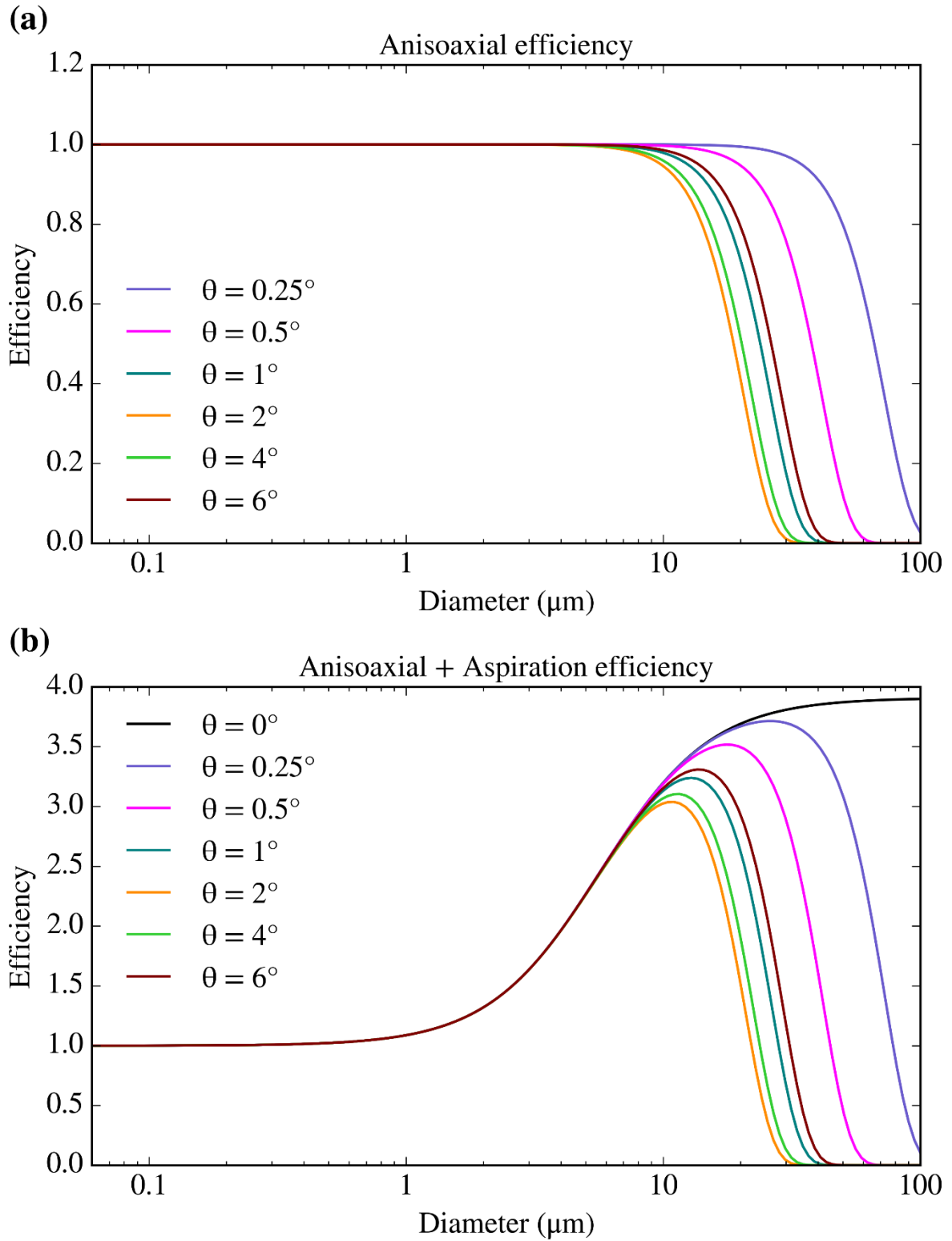
1020
1021   Fig. 3. Anisoaxial inertial losses of the sampling carried out by the Filters inlet system for different values of the angle in
1022   between the inlet and the flight direction. The calculations have been presented by themselves (a) and combined with the
1023   aspiration efficiency (b), which one can see in Fig. 2a. The anisoaxial calculations have been done using the equations given
1024   by (Hangal and Willeke, 1990b), using the same parameters and dimensions than in Fig. 2, apart from the flow rate, which
1025   was set to 65 L min^{-1} in order to be within the valid range of U/U_0 that was used to develop the equation. For smaller or
1026   larger values of the flow rate (under which most of the sampling is carried out), the differences in the efficiency from the
1027   ones show here are minimal.
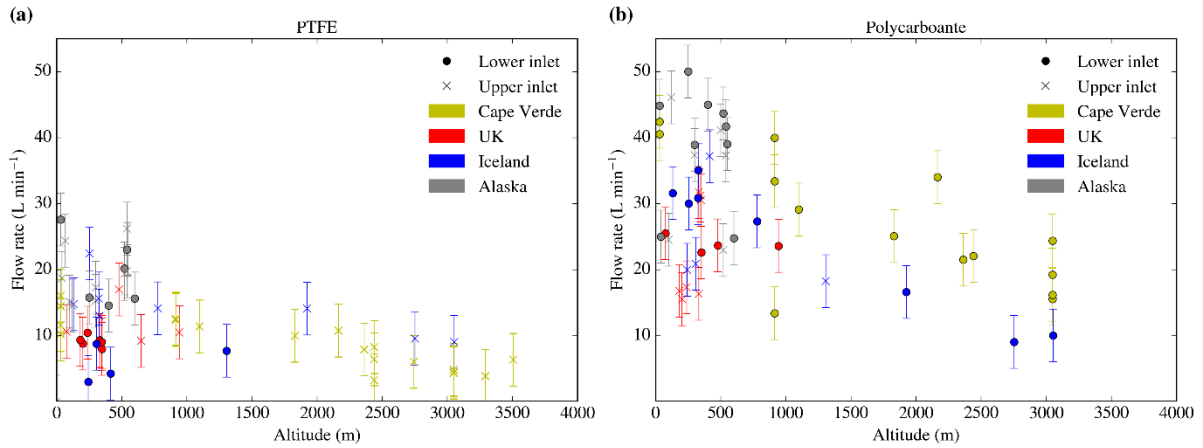
1028
1029 Figure 4. Filter flow rate of different samplings carried out in different campaigns at each altitude using: (a) Sartorius PTFE
1030 membrane filters (47mm diameter with a pore size of 0.45µm) and (b) Whatman nucleopore polycarbonate track etched
1031 filters (47mm diameter with a pore size of 0.4µm). The crosses represent samples taken in the upper line of the inlet system,
1032 whereas dots represent the sampling in the bottom line. Different mesh supports were used for the data collection. The data
1033 from Cape Verde was extracted from (Price et al., 2018) and the notes of the analysis carried out by the authors whereas the
1034 altitude data from the other three was obtained from the pressure altitude measurement carried out by the Reduced Vertical
1035 Separation Minimum system on board of the aircraft. The altitude data was extracted from the FAAM core datasets C019,
1036 C022, C024, C025, C058, C059, C060, C061, C062, C063, C085, C086, C087, C088, C089, C090 and C091 (via the Centre for
1037 Environmental Data Analysis). The bypass was closed for all the data in Cape Verde whereas it was open for all the data in
1038 the other campaigns. Note that the flow rate here corresponds to the filter flow rate (measured with the mass flow meter),
1039 not the total one.

1040
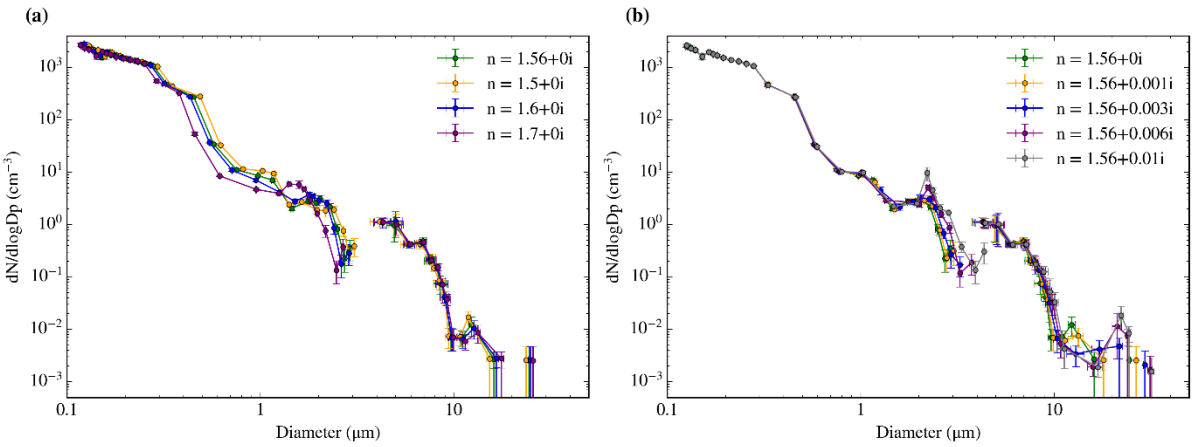
1043 Figure 5. Sensitivity of the size distributions measured by the PCASP-CDP during the C010 flight on the 2017/05/10 from
1044 11:24 to 11:38 UTC to small variations in the refractive index. We tested both the real part (a) and imaginary part (b). The
1045 errors are calculated according to the methods explained in Sect. 3.

1046

1047
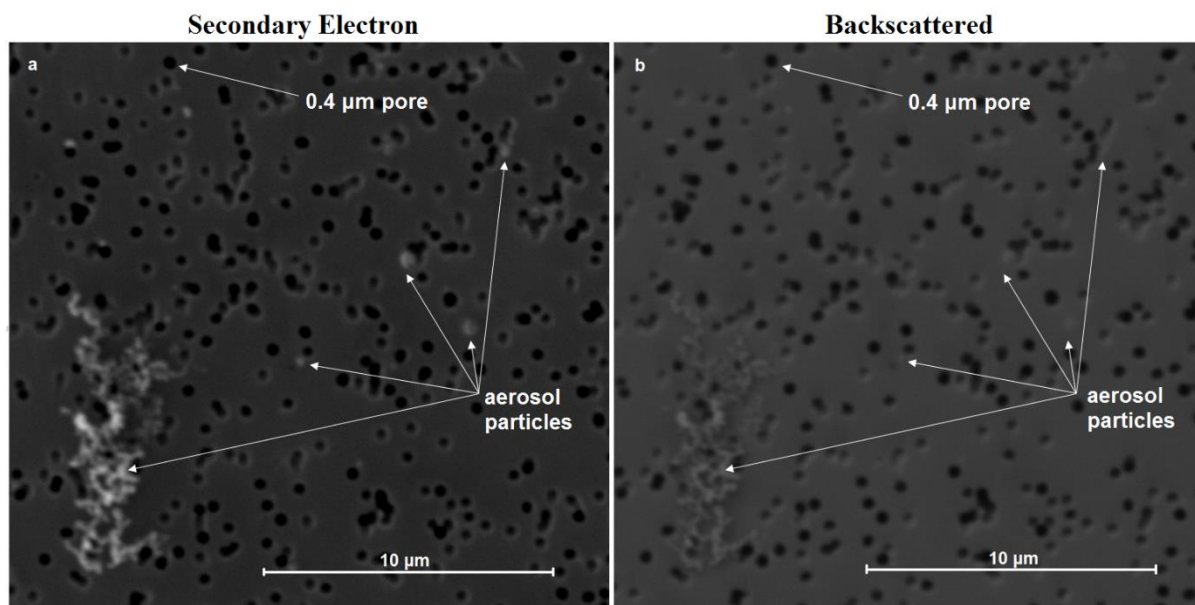
1048 Figure 6. Secondary electron image (a) and Back Scattered Electron image (b) of the same area of the same filter, collected
1049 in S.E. England on the 2018/07/05 from 13:32 to 13:47 in the upper line with the bypass open. As one can see, some of the
1050 small particles in the SE image appear almost transparent under the BSE image. Even the 10µm soot particle in the bottom
1051 left of the image shows a very low contrast in the BSE image.

1052

1053
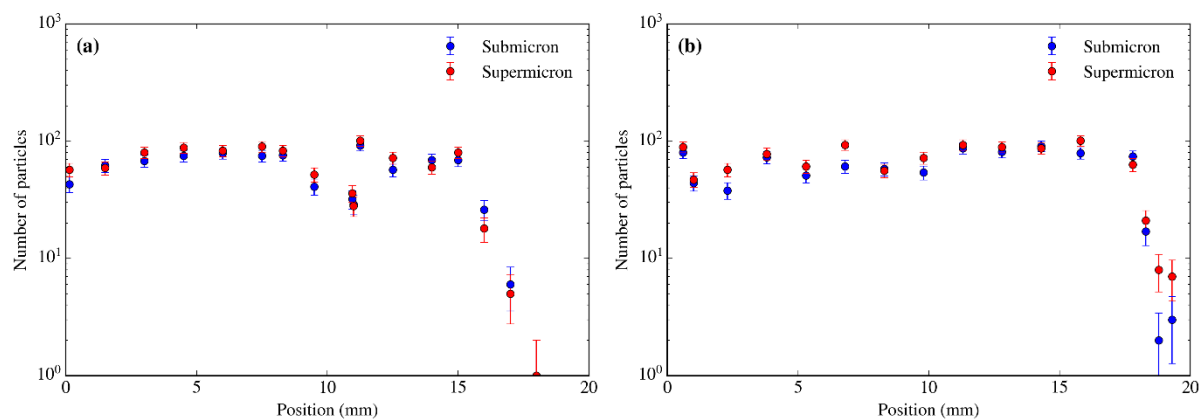
Figure. 7. Radial distribution of particles test on the sample collected on the 2017/10/02 (flight C059) from 16:24 to 16:40 UTC about 320 m high in south Iceland, using the lower line and open bypass, sampling 432 L. Number of submicron and supermicron particles in same size areas (~160x190 μm²) radially distributed versus the distance from the approximate centre through a radius of the filter (a) and another trajectory from the centre of the filter deviated 30° from the first radius (b). The analysis was done at 20 KeV and x5000. The number of both supermicron and submicron particles remains very constant all over the surface of the filter, until reaching the edges of it (which are cover by a rubber O-ring during the sample) and the number of particles drops to the limit of the detection within a few millimetres. The error in the number of particles comes from Poisson counting statistics.

1062

1063

1064

1065
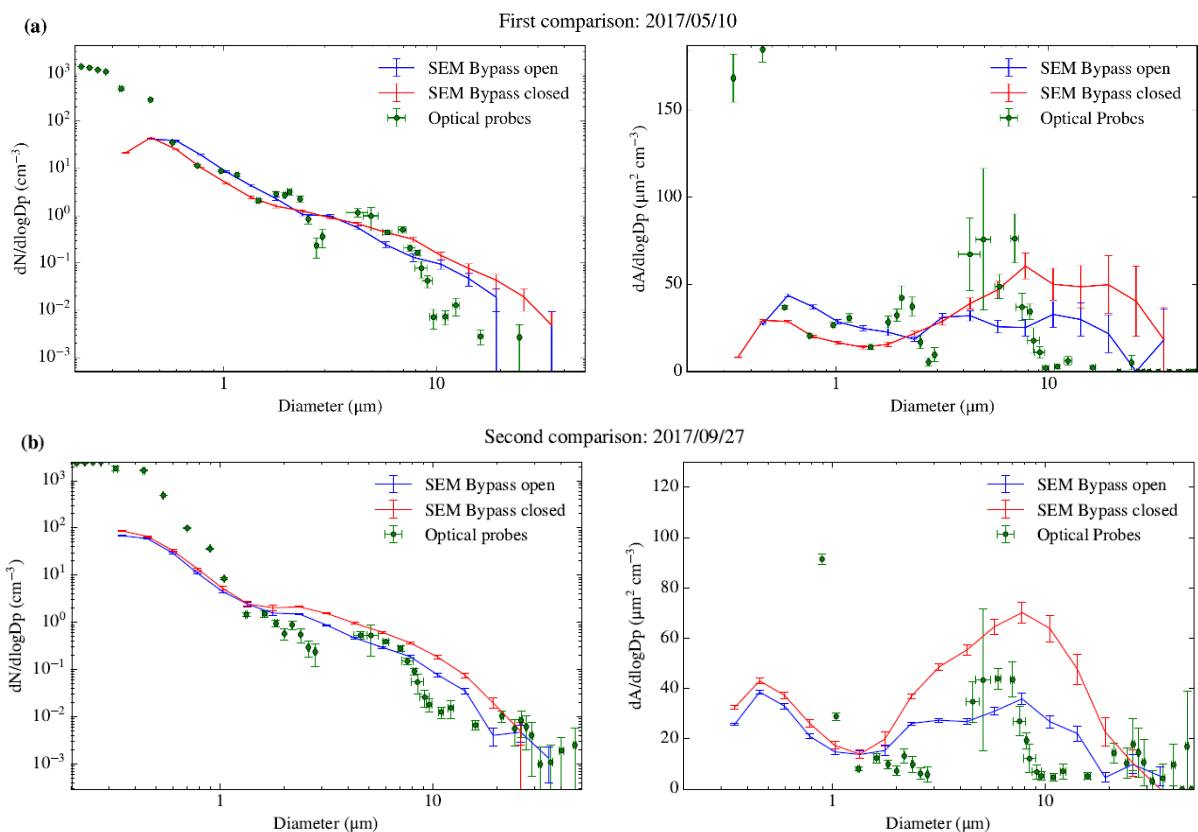
1066
1067 Figure 8. (a) First bypass test carried out during the C010 flight on the 2017/05/10 from 11:24 to 11:38 UTC. The lower line
1068 sampled 226 L with the bypass closed, whereas the upper line sampled 141 L with the bypass open at an altitude of about
1069 150 m. The flow rates were 16.1 L min^{-1} and 10.6 L min^{-1} respectively. (b) Second bypass test carried out during the C057
1070 flight on the 2017/09/27 from 13:33 to 13:50 UTC. The lower line sampled 555 L with the bypass open, whereas the upper
1071 line sampled 499 L with the bypass closed, at about 240 m. The flow rates were 34.7 L min^{-1} and 31.2 L min^{-1} respectively.
1072 The position of the closed and open line was swapped with respect to the first comparison. The sampling was interrupted
1073 for a minute to avoid a turn. Both comparisons are shown in both number size distribution and surface area size distribution.
1074 The optical probes are the PCASP-CDP, using the closest calibration to the sampling date and a refractive index of 1.56 as
1075 stated in the Sect. 2.3. The only error source considered for the SEM size distribution is the Poisson counting error.

1076

1077

1078
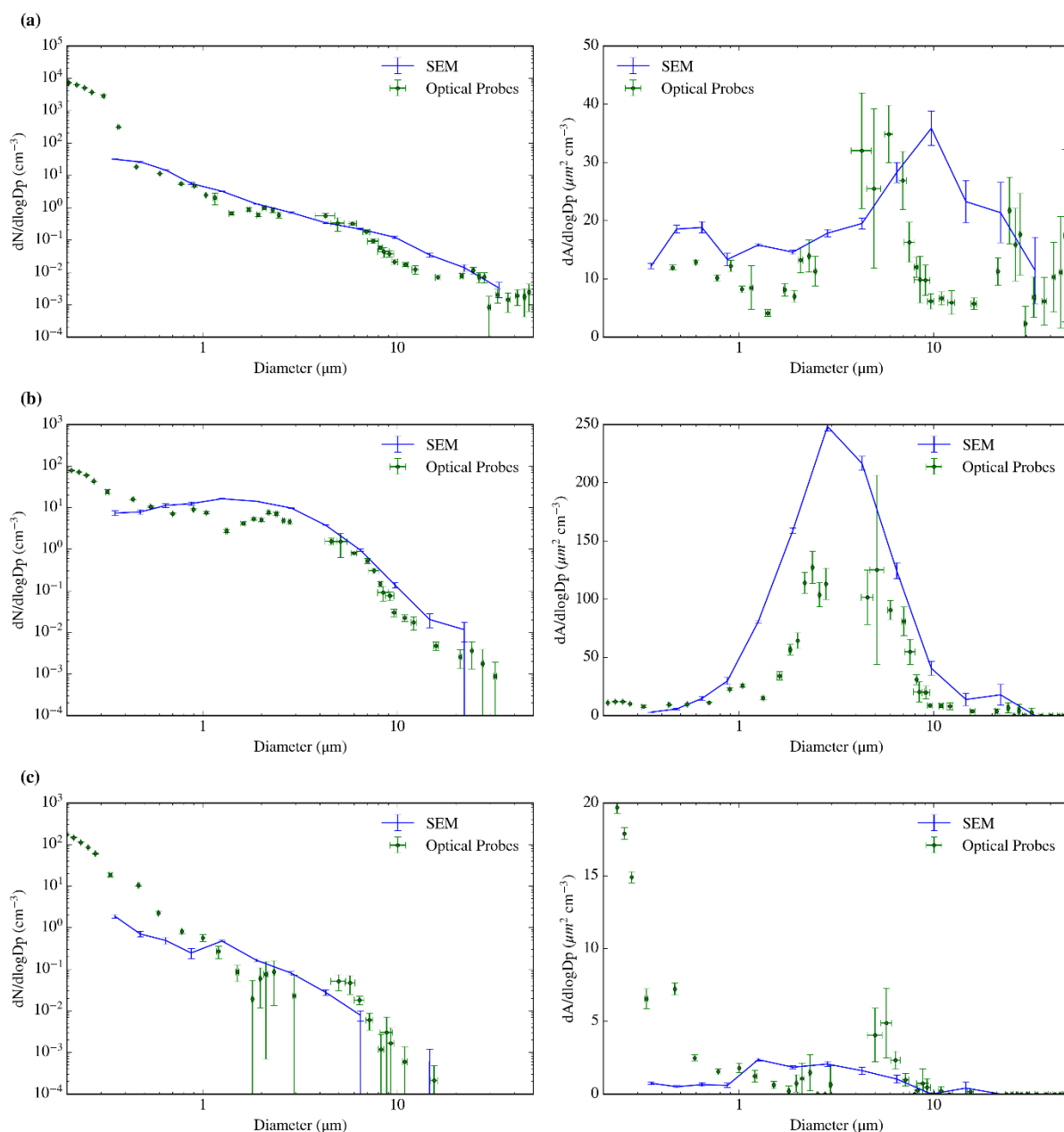
Figure 9. SEM obtained size distribution compared with PCASP-CDP online size distribution for three different sampling periods in three different aerosol environments. Close to London, on the 2017/07/19 (flight C024) from 15:20 to 15:51 UTC, sampling 953 L (a), south of Iceland on the 2017/10/02 (flight C059) from 16:24 to 16:40 UTC, sampling 432 L at an altitude of about 320 m, (b) and in north Alaska on the 2018/03/20 (flight C090) from 20:15 to 20:37, sampling 724 L (c). All the sampling was done in the upper line with the bypass open. The flow rates through the filter holders are 30.9, 30.5 and 42.0 L min^{-1} respectively. The optical probes are the PCASP-CDP, using the closest calibration to the sampling date and a refractive index of 1.56 as stated in Sect. 2.3.

(b)

1093

(c)

1094
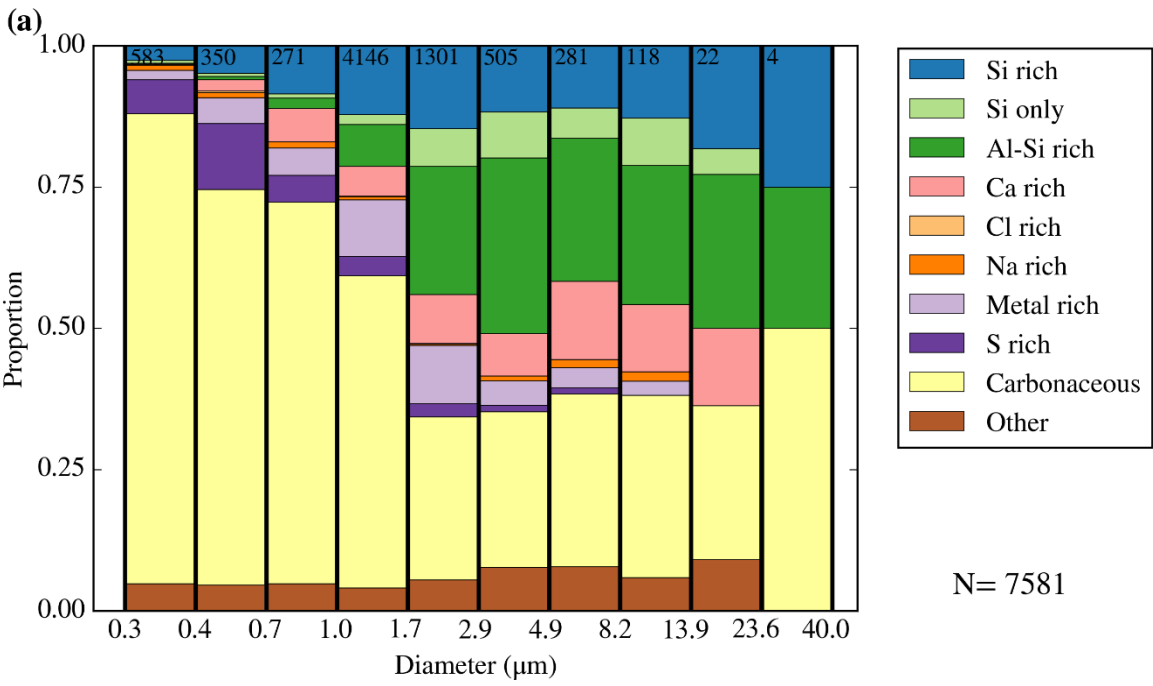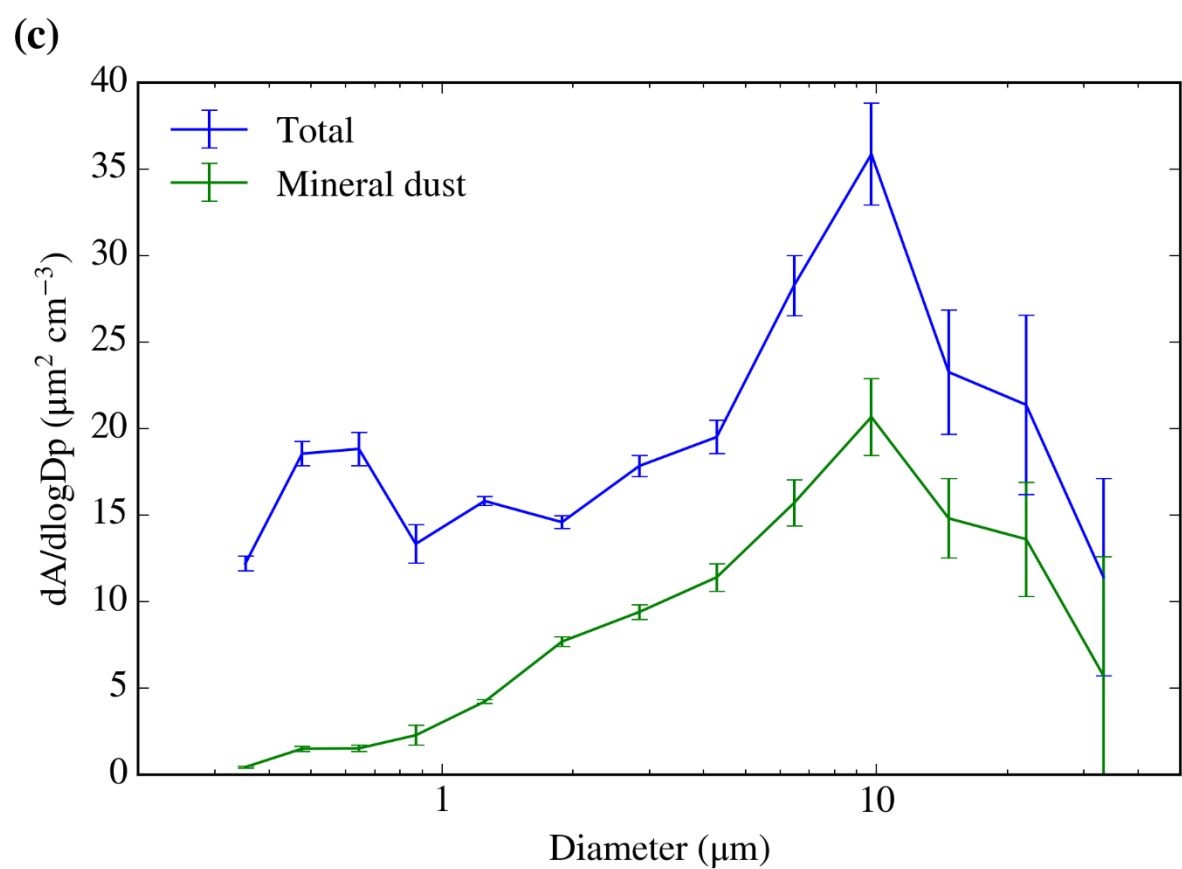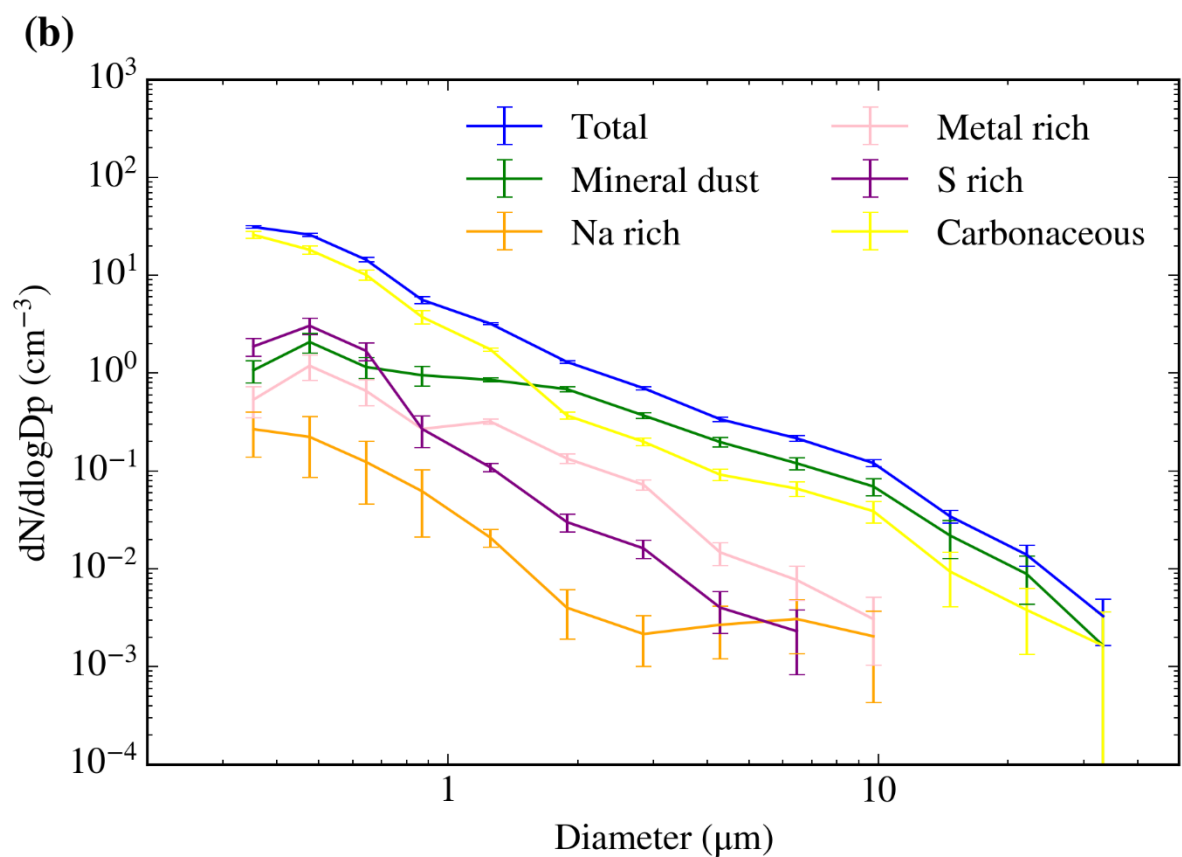
1095 Figure 10. Size-segregated compositional and morphological analysis of a sample collected close to London (S.E. England) on
1096 the 2017/07/19 from 15:20 to 15:52 UTC by the lower line with the bypass open, sampling a total of 953L at 350 m altitude.

(a) Fraction of particles corresponding to each compositional category (described in the Appendix B) for each size. The number of particles per bin can be seen in the top of the figure. (b) Number size distribution for each composition. Cl rich particles were not included since only two particles in this category were found. The errors have been calculated from the Poisson counting statistics (applying it to both the size distribution and the compositional measurements). (c) Surface area of both all the detected aerosol particles and the ones whose composition was consistent with mineral dust. Errors have been calculated in the same way as before. By integrating the green curve in the figure (c) we obtained the total surface area of mineral dust in the sample (19.1 μm^2 cm^{-3}).
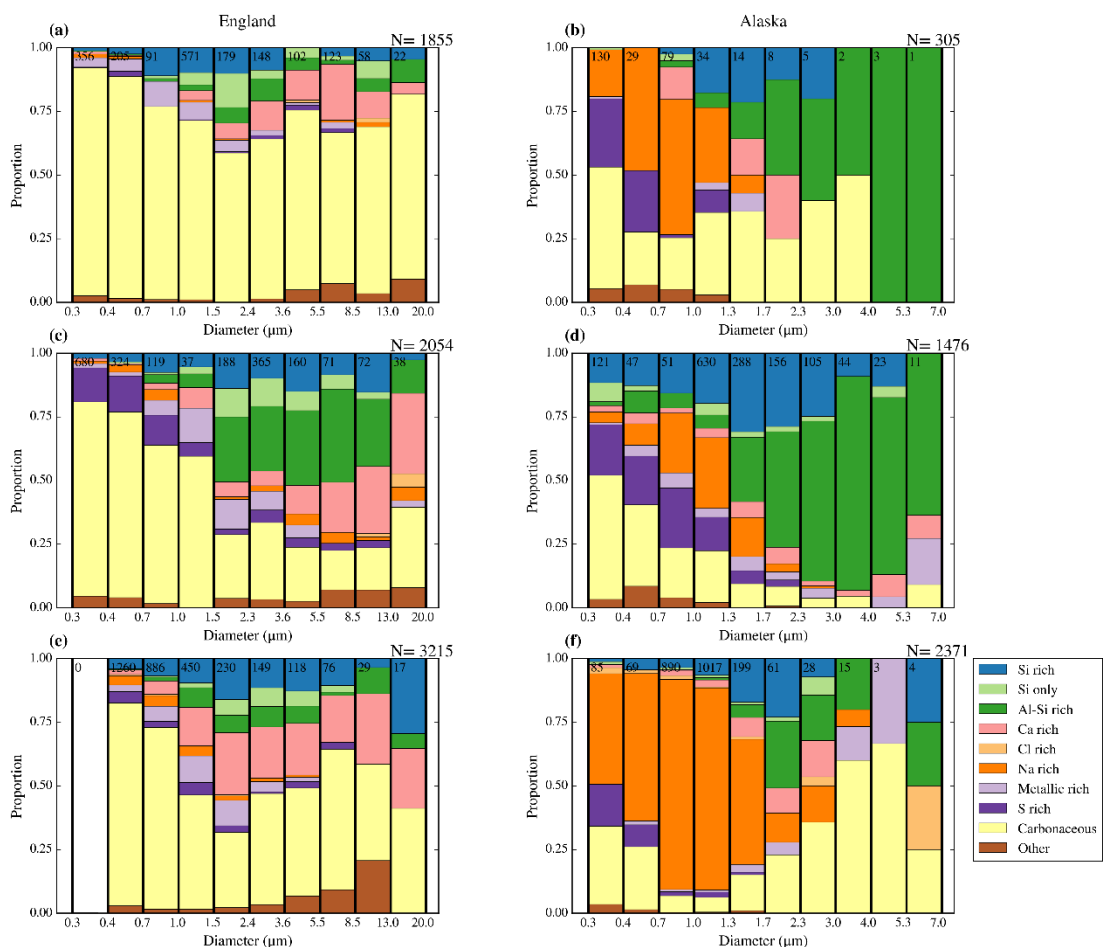
Figure 11. Six examples of the size resolved composition of aerosol sampled from the BAe-146 aircraft above South England (a, c and e) and North Alaska (b, d and f). All the samples were taken with the bypass open. The dates and sampling times (in UTC) are: (a) 2017/07/17 (flight C022) from 9:29 to 9:41, sampling a total of 182 L at an altitude of about 240 m, (b) 2018/03/18 (flight C089) from 19:28 to 19:48, sampling a total of 404 L at an altitude of about 600 m, (c) 2017/07/19 (flight C024) from 15:20 to 15:52, sampling a total of 256 L at an altitude of about 350 m (this sample was taken on the same that as the one shown in Fig. 10), (d) 2018/03/20 (flight C090) from 20:15 to 20:37, sampling a total of 724 L at an altitude of about 520 m, (e) 2017/07/20 (flight C025) from 12:51 to 13:09, sampling a total of 425 L, (f) 2018/03/21 (flight C091) from 18:27 to 18:56, sampling a total of 1187 L at an altitude of about 120 m at an altitude of about 940 m.

1114
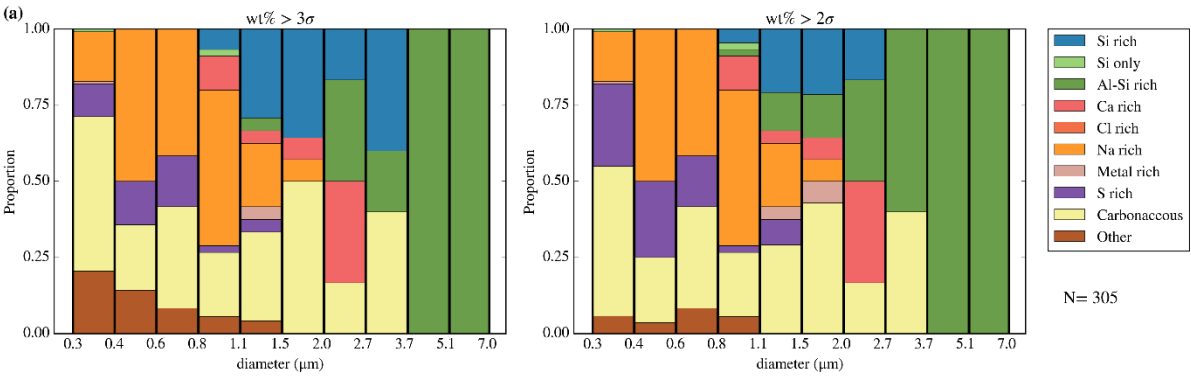
1115
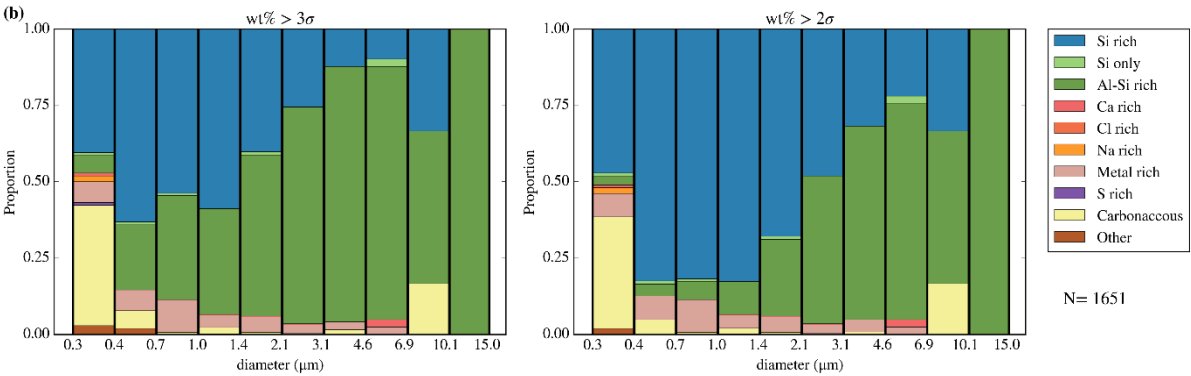
1116

1117 Figure C1. Size-segregated composition of two aerosol samples for different element detection confidence levels. The
1118 samples are 2018/03/18 from 19:28 to 19:48 UTC in north Alaska (a) and 2017/10/02 from 16:24 to 16:40 UTC in Iceland (b).
1119 The two samples are very different since the first sample presented a very low aerosol loading and it is dominated by Na rich
1120 particles, Carbonaceous and mineral origin aerosol (Si rich, Si only, Al-Si rich) with significant contributions of S rich particles
1121 whereas the second sample presented a high aerosol loading and it was mainly dominated by mineral origin aerosol. The
1122 different in the confidence mainly affected the Si and Al-Si rich particles as well as the S rich particles in the sample (a),
1123 whereas it only affected the Si and Al-Si rich particles in the sample (b).

1124